

Temporal variations in storage conditions of the post-collapse rhyolites, Valles Caldera, New Mexico (USA)

Magdalen A. Grismer* and D Laura E. Waters

Department of Earth and Environmental Science, New Mexico Institute of Mining and Technology, Socorro, NM 87801, USA.

ABSTRACT

We present a petrologic study of the post-collapse rhyolites from Valles Caldera (New Mexico, USA) to evaluate changes in magmatic storage conditions following the eruption of the Upper Bandelier Tuff (UBT). We assess likely phenocrysts through textures, comparison with experiments, and rhyolite-MELTS outputs, and apply thermobarometers, oxygen barometers, and hygrometers to these minerals. The post-collapse rhyolites have average pre-eruptive temperatures ranging from 742-824 °C, average pre-eruptive oxygen fugacities ranging from -0.1 to +1.3 Δ NNO, and average pre-eruptive H₂O contents ranging from 4.4-6.0 wt% H₂O. Average storage pressures range from 130-196 MPa for all rhyolites except the youngest, which has a range of 157-376 MPa. The post-collapse rhyolites are more oxidizing than the UBT and have similar pre-eruptive pressures. The change in oxidation state between the rhyolites and UBT, despite similar storage pressures, can be explained if the UBT is generated from a unique, reduced source but accumulated at depths similar to the post-collapse rhyolites.

KEYWORDS: Valles Caldera; High-silica rhyolite; Petrology; Thermobarometry; Oxygen barometry.

1 Introduction

Caldera-forming eruptions are some of the largest on Earth [10¹-10³ km³; Mason et al. 2004; Cole et al. 2005] and are sourced from voluminous, silica-rich magmas that develop in the upper crust [Hildreth et al. 1991; Wilson et al. 1995; Coombs and Gardner 2001; Hildreth 2004; Hildreth and Wilson 2007]. Resurgent caldera systems are those systems that have experienced uplift in the caldera floor and post-collapse volcanism [Smith and Bailey 1968] and offer a unique opportunity to understand how silicic magmas develop and accumulate in the crust during time periods following and/or preceding the emplacement of a voluminous ignimbrite [Cole et al. 2005; Geshi 2020]. In general, post-collapse eruptions appear to differ from their preceding caldera-forming eruptions in numerous ways, ranging from changes to magmatic flux (e.g. eruptive volumes) to differing pre-eruptive intensive variables (e.g. temperature, oxygen fugacity, and pressure), where these variations hold essential information on changes to the overall magmatic system. At Long Valley Caldera, the Early Rhyolites erupted 17 ka after the Bishop Tuff and continued erupting for the next 90 ka. The Early Rhyolites have higher temperatures (752-844 °C) and reduced oxygen fugacities (\sim -0.3 to -0.7 Δ NNO, where Δ NNO is the logfO₂ of the sample $-\log fO_2$ of the nickel-nickel oxide buffer at a given temperature), when compared to the caldera-forming Bishop Tuff [700–820 °C and -0.6 to +0.6 ΔNNO; Hildreth et al. 2017]. Hildreth et al. [2017] suggest that the change in oxidation state could be explained by interaction of graphitebearing roof rocks with the magma body beneath Long Valley prior to eruption, which implies that interaction of the country rock with the Long Valley caldera system may play an important role in the formation of the Early post-collapse rhyolites. As another example, the East Biscuit Basin flow at Yellowstone Caldera erupted following the caldera-forming Lava Creek Tuff and contains low $\delta^{18}O$ glass, quartz, sanidine,

and zircon (where $\delta^{18}O$ is defined as $1000(^{18}O/^{16}O_{sample}-^{18}O/^{16}O_{SMOW})/^{18}O/^{16}O_{SMOW}$ and SMOW is defined as standard mean ocean water), which indicates significant interaction with hydrothermally altered crust [Bindeman and Valley 2000; Girard and Stix 2009] in post-collapse rhyolites. Thus, the chemistry of post-collapse volcanism at Long Valley and Yellowstone Calderas suggests that interaction with the country rock may play a greater role in the post-collapse magmatism than the caldera-forming eruptions.

Valles Caldera, a resurgent caldera system, has sourced both voluminous, caldera-forming rhyolites and smaller, effusive, post-collapse eruptions of high-silica and low-silica rhyolite (HSR and LSR, respectively). The 1.256 ± 0.010 Ma [Phillips et al. 2007] Upper Bandelier Tuff (UBT) is the final caldera forming eruption at Valles Caldera and has been the focus of geologic studies for the past 40 years. The eruptive ages, storage conditions, and volatile contents of the UBT have been well constrained through isotopic work, geochemical and petrologic studies, as well as melt inclusion studies [e.g. Kuentz 1986; Skuba 1990; Dunbar and Hervig 1992; Phillips et al. 2007; Wilcock et al. 2013; Wolff and Ramos 2014; Wolff et al. 2015; Cook et al. 2016; Boro et al. 2020; Waelkens et al. 2022]. Similarly, the most recent post-collapse eruptions that constitute the East Fork Member [74.4-68.7 ka; Wolff et al. 2011; Nasholds and Zimmerer 2022 have been studied to constrain their eruptive ages, storage conditions, and petrogenesis [e.g. Self et al. 1988; Wolff and Gardner 1995; Zimmerer et al. 2016; Ren and Parker 2019: Eichler and Spell 2020l. The Redondo Creek and Valle Grande Members, which erupted between the UBT and East Fork Member from 1199-529.3 ka, have newly determined eruptive ages [Nasholds and Zimmerer 2022] and existing geochemical and isotopic data [Spell and Kyle 1989; Spell et al. 1993, but lack estimates of their pre-eruptive storage conditions using mineral-melt thermobarometry.

Here, we conduct a petrologic and geochemical study to evaluate the intensive variables of the post-collapse rhyolites that erupted from 1200–68.7 ka (Redondo Creek, Cerro Del Medio, Cerro Del Abrigo, Cerro Santa Rosa, Cerro San Luis, Cerro Seco, San Antonio, South Mountain, and Banco Bonito; Figure 1). We use these data to evaluate changes to the magmatic storage conditions (temperature, oxygen fugacity, H_2O contents, and pressures) that accompany chemical changes in post-caldera volcanism to better understand the evolution of the Valles Caldera plumbing system since the eruption of the UBT.

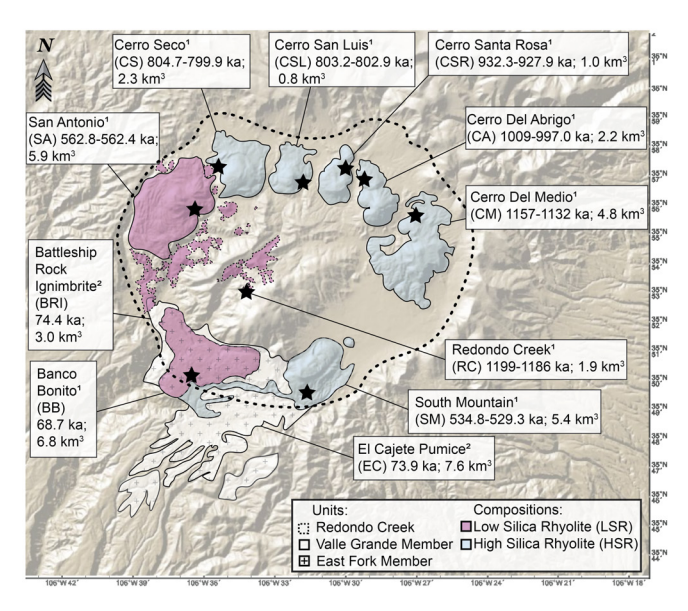


Figure 1: The erosional remnant of Valles Caldera (thick dashed line) is shown along with the post-collapse rhyolites, with estimated erupted volumes and ages from (1) Nasholds and Zimmerer [2022] and (2) Wolff et al. [2011]. Map symbology defines eruptive units, their compositions, and sample locations from this study. Redondo Creek is outlined with a thin dashed line as the eruption did not form a single dome. The Valle Grande Member eruptions are shown with a solid black outline and the East Fork Member is shown with a cross pattern to differentiate the eruptive units. Rhyolites with compositions corresponding to HSRs are shown in pale blue and LSRs are shown in pink. Black stars indicate sample locations. The base DEM was made using GeoMapApp [Ryan et al. 2009].

2 GEOLOGIC BACKGROUND

The Jemez Mountains volcanic field (JMVF), in north-central New Mexico (USA) marks the intersection of the north-east south-west trending Jemez Lineament, with the north-south trending Rio Grande Rift. The Jemez Lineament runs parallel to the shallow angle suture zone between the Proterozoic Yavapai and Mazatzal provinces, where the weaker crust provides a conduit for magma [Shaw 1999; CD-ROM working group 2002; Magnani et al. 2004; Ricketts et al. 2016]. In the last ~13 Ma, the JMVF has erupted a series of tholeitic and alkaline basalts, dacitic to andesitic lavas (e.g. Santa Fe group, Paliza Canyon formation, Tschicoma dacites), which were ultimately followed by rhyolite eruptions [Wolff et al. 2005; Broxton et al. 2007; Kelley et al. 2013; Wu et al. 2021].

Valles Caldera and the surrounding area are blanketed by two voluminous ignimbrites, the 1.256 \pm 0.010 Ma UBT and

 1.60 ± 0.02 Ma LBT, which have a cumulative erupted volume of ~800 km³ [Phillips et al. 2007; Goff et al. 2014; Wolff and Ramos 2014; Cook et al. 2016]. The UBT is a zoned eruption of five different rhyolite units that range in composition from HSR to LSR, with crystallinities ranging from ~5–25 vol% [Balsley 1988; Wilcock et al. 2013; Goff et al. 2014]. The UBT mineralogy includes sanidine, plagioclase, fayalite, biotite, clinopyroxene, orthopyroxene, hornblende, and Fe-Ti oxides Balsley 1988; Wilcock et al. 2013; Goff et al. 2014]. Previous petrologic work suggests that the pre-eruptive temperatures range from ~700–837 °C, with the last erupted unit being the hottest Balsley 1988; Warshaw and Smith 1988; Wilcock et al. 2013]. Oxygen fugacities (fO_2) for four of the five units in the UBT are reduced, with their fO2 values close to the QFM (quartzfayalite-magnetite) buffer, whereas the last erupted unit is oxidized, with an fO2 near the NNO buffer [Warshaw and Smith 1988]. Volatile contents range from 2.8–5.0 wt% H₂O and 29– 147 ppm CO₂, which correspond to pressures of 100–143 MPa and depths of ~3.8 to 5.4 km based on a crustal density of 2700 kg m⁻³ [Dunbar and Hervig 1992; Waelkens et al. 2022].

Following the eruption of the UBT, post-caldera resurgence began with the Deer Canyon Member, which includes small volume rhyolite lavas and lithic tuffs [Spell and Kyle 1989; Spell and Harrison 1993; Spell et al. 1996; Goff et al. 2011]. The eruptive span of Deer Canyon rhyolite begins a maximum of 11.1 ka after the eruption of the UBT based on recent $^{40}\mathrm{Ar}/^{39}\mathrm{Ar}$ age dating on post-collapse rhyolite lavas and domes [Phillips et al. 2007; Nasholds and Zimmerer 2022]. Central dome resurgence continued with Redondo Creek, which is a small volume (1.9 km³) of low-silica rhyolite erupted over a period of 13.1 ka (Figure 1), with the oldest lavas dated at 1199 ka [Smith and Bailey 1968; Nasholds and Zimmerer 2022].

The Valle Grande Member erupted following the Deer Canyon and Redondo Creek rhyolites. The Valle Grande Member is comprised of the following rhyolite domes: Cerro Del Medio, Cerro Del Abrigo, Cerro Santa Rosa, Cerro San Luis, Cerro Seco, San Antonio, and South Mountain (Figure 1), which erupted from 1158-528 ka [Spell and Kyle 1989; Spell and Harrison 1993; Spell et al. 1993; Nasholds and Zimmerer 2022]. The Valle Grande rhyolites decrease in age in a counterclockwise direction around the edge of the caldera (Figure 1). starting with Cerro Del Medio. Cerro Del Medio erupted from 1157–1132 ka with an eruptive volume of 4.8 km³ and is primarily an HSR obsidian dome [Nasholds and Zimmerer 2022]. Cerro Del Abrigo then erupted from 1009–997.0 ka and is 2.2 km³ of glassy, crystal-rich HSR [Figure 1; Nasholds and Zimmerer 2022]. Next, Cerro Santa Rosa erupted from 932.3-927.9 ka and is another crystal-rich HSR, with a small eruptive volume of 1.0 km³ [Figure 1; Nasholds and Zimmerer 2022]. Cerro San Luis and Cerro Seco overlap in their eruptive ages (803.2-802.9 ka and 804.7-799.9 ka, respectively) but are distinct crystal-rich HSRs with volumes of 0.8 km³ and 2.3 km³, respectively [Figure 1; Nasholds and Zimmerer 2022]. A brief hiatus of 237 ka preceded the eruption of San Antonio, a larger (5.9 km³) crystal-rich LSR that erupted from 562.8-562.4 ka [Figure 1; Nasholds and Zimmerer 2022]. The final dome of the Valle Grande member is South Mountain, which erupted from 534.8–529.3 ka and is a 5.4 km³ crystal-rich HSR [Figure 1; Nasholds and Zimmerer 2022]. The Valle Grande rhyolites are crystal-rich and contain sanidine, plagioclase, and quartz, and include trace oxides, biotite, and hornblende [Spell and Kyle 1989]. The existing temperature estimates from Spell and Kyle [1989] based on feldspar thermometry vary from 724–808 °C. Spell and Kyle [1989] also utilize hornblende barometry to calculate a pressure range of 95–104 MPa; however, they note a minimum error of ±100 MPa and acknowledge the potential for a range of pre-eruptive pressures wider than their findings.

After a 453 ka period of guiescence, El Cajete erupted followed by the Battleship Rock Ignimbrite and Banco Bonito; these three units collectively form the East Fork Member, located on the south-western wall of the caldera [Figure 1; Wolff and Gardner 1995; Zimmerer et al. 2016; Eichler and Spell 2020; Nasholds and Zimmerer 2022]. Banco Bonito is the youngest eruption at Valles Caldera at 68.7 ka, with an eruptive volume of 6.8 km³ of glassy LSR [Wolff and Gardner 1995; Goff 2010]. The East Fork Member contains more abundant plagioclase than the previously erupted rhyolites, but also includes sanidine, quartz, and a comparatively higher percentage of biotite, hornblende, and pyroxenes [Spell and Kyle 1989; Eichler and Spell 2020]. There are two petrologic studies of the East Fork Member that utilize Fe-Ti oxide, two-feldspar, and clinopyroxene thermometry and find a range of pre-eruptive temperatures from 789-868°C [Ren and Parker 2019; Eichler and Spell 2020]. Ren and Parker [2019] find pressures in the East Fork Member vary from 196-438 MPa (~9-19 km deep), based on the hornblende barometry models of Hammarstrom and Zen [1986] and Hollister et al. [1987]. Ren and Parker [2019] also apply the quartz, ulvospinel, ilmenite, fayalite (QUILF) equilibrium model of Andersen et al. [1993] to clinopyroxene, orthopyroxene, ilmenite, and magnetite in the East Fork Member to find oxidizing conditions with fO2 ranging from +1.0 to +1.5 log units greater than the NNO buffer [Ren and Parker 2019].

The notable differences between the caldera-forming eruption of the UBT and the post-collapse eruptions at Valles Caldera are the absence of fayalite in the post-collapse eruptions and the apparent trend of increasing temperature and increasing oxidation state, where mineral phases in the East Fork Member record the hottest temperatures and the most oxidizing conditions (which is consistent with the absence of fayalite). We can understand when the shift to elevated temperatures and oxidizing conditions occurred in Valles Caldera by determining the pre-eruptive intensive variables for the Valle Grande rhyolites and evaluating those conditions as a function of their newly published, revised eruptive ages [Nasholds and Zimmerer 2022].

3 METHODS

The Valles Caldera National Preserve and the New Mexico Bureau of Geology and Mineral Resources (NMBG) provided samples for each post-collapse rhyolite (Figure 1, stars; Table 1; see sampling notes in Supplementary Material 1). We cut thin sections to reflect the overall mineralogy of each rhyolite by selecting areas of the rock that included all the minerals

seen in hand samples. We collected 30-40 photomicrographs of each thin section with an Infinity microscope camera and Olympus CX31 petrographic microscope to merge them into \sim 5×5 cm² photomosaics using Adobe Photoshop. We determined mineral abundances for each sample by point counting 1000 counts in duplicate per slide using a Pelcon automatic point counter; we report the average values of the totaled 2000 counts per slide. We powdered chips of the samples using a tungsten carbide shatter box and sent aliquots to Activation Laboratories Ltd. in Ancaster, Ontario (Canada), to obtain major and trace element abundances via inductively coupled plasma optical emission spectroscopy (ICP-OES) and inductively coupled plasma mass spectroscopy (ICP-MS) (Activation Labs analysis type 4Litho). We used the Cameca SX-100 electron microprobe at NMBG with an accelerating voltage of 15 kV and a probe current of 20 nA for all crystal analyses. For feldspar, Fe-Ti oxides, and mafic silicates, we used spot sizes of $5 \, \mu m$, $< 1 \, \mu m$ to $10 \, \mu m$, and $< 1 \, \mu m$ (where $< 1 \, \mu m$ corresponds to a setting of 0 µm), respectively. We used an accelerating voltage of 15 kV, a probe current of 5 nA, and a spot size of 7 µm for glass analyses. We used time dependent intensities to correct for Na mobility in the glasses during glass analyses. Backscatter electron (BSE) microprobe images were collected during analyses. We collected individual point analyses on Fe-Ti oxide, biotite, hornblende, and pyroxene phenocrysts, and when size permitted, we collected point analyses on transects from core to rim on feldspars and hornblendes to quantifu crustal compositions. Transects were selected to include any compositional variation seen in BSE and to avoid melt inclusions when present. Spacing intervals for each transect range from 10–60 μm depending on the size of the crystal and zoning, if present. All calibration standards, microprobe settings (crystals and spectrometers), and analyses of secondary standards are reported in Supplementary Material 2 Table S1. Analyses matched microprobe standards for major elements with a range of 0.07-6.3% relative error, where error is greatest when elemental concentrations are ≤1 wt%. We checked all analyses against reference standards suited to the material (e.g. rhyolite glass VG-568 for glass analyses), and a kaersutite standard was used to analyze overall performance of the microprobe.

4 RESULTS

4.1 Petrography

All post-collapse rhyolites, except for the samples from Banco Bonito and Cerro Del Medio, contain sanidine + quartz + anorthoclase/plagioclase + biotite + hornblende + magnetite + ilmenite ± clinopyroxene ± orthopyroxene ± apatite, with trace rare earth element bearing minerals including zircon and chevkinite (Table 1 and Figure 2; in Table 1 and subsequent tables we order the post-collapse rhyolites from oldest to youngest reading left to right). We observed all the above minerals except for sanidine and chevkinite in the youngest unit, Banco Bonito (Table 1). The rhyolite obsidian from Cerro Del Medio is nearly aphyric, with trace oxides and sanidine, plagioclase, and biotite microlites (Table 1 and Supplementary Material 3 Figure S1). Redondo Creek, Cerro Del Medio,

Dome[†] RC **CSR CSL** CS SA SM BB CMCA Sanidine 3.05 0.00 12.7 12.7 13.2 7.50 6.39 5.45 Sanidine microlites 0.30 2.40 0.84 0.69 0.31 0.10 0.30 0.85 Plagioclase[‡] 4.20 7.40 0.10 3.80 4.548.05 7.47 4.90 5.12 Plagioclase microlites[‡] 0.60 0.55 0.05 0.35 0.41 0.58 0.700.46 0.60 Quartz 5.15 < 0.10 5.20 4.24 8.50 3.12 2.40 5.25 1.70 Quartz microlites 0.55 0.70 0.450.45 0.31 0.65 0.75 0.41 0.40 Fe-Ti oxides (magnetite & ilmenite) 0.95 0.20 0.32 0.90 0.71 0.36 0.85 0.82 1.10 Biotite 3.85 0.10 0.50 0.55 0.10 0.21 2.15 88.0 2.75 Clinopyroxene 0.30 < 0.10 < 0.10 < 0.10 < 0.10 0.35 0.95 Hornblende < 0.10 < 0.10 0.75 0.20 0.10 0.11 < 0.10 0.31 0.65 tr§ Zircon tr tr tr tr tr tr tr tr Glass|| 75.8 95.8 79.2 75.9 71.5 76.7 74.0 77.6 86.7 Total 100 100 100 100 100 100 100 100 100 Crystalline inclusions[¶] 4.50 Vesicles 1.4 0.10 2.75 1.10 7.04 6.00 1.75 2.95 0.25

Table 1: Mineral phase proportions, normalized without vesicles*.

*Determined through 1000 counts per sample, in duplicate. †RC – Redondo Creek, CM – Cerro Del Medio, CA – Cerro Del Abrigo, CSR – Cerro Santa Rosa, CSL – Cerro San Luis, CS – Cerro Seco, SA – San Antonio, SM – South Mountain, BB – Banco Bonito. ‡At the time point counts were completed we did not have electron microprobe analyses so used the term plagioclase as a catch-all for any feldspars that were not sanidine. §tr – trace abundance. || Redondo Creek samples contained devitrified glass that was counted as glass here. ¶Crystalline inclusions are aggregates of crystals that include plagioclase, hornblende, clinopyroxene, and biotite.

Cerro Del Abrigo, Cerro Santa Rosa, Cerro San Luis, Cerro Seco, San Antonio, South Mountain, and Banco Bonito range from 13.3–28.5% crystallinity (Table 1 and Supplementary Material 3 Figure S1). All the samples have glassy groundmasses, except for the sample from Redondo Creek which has a devitrified matrix. Sanidine, anorthoclase, plagioclase, and quartz constitute 77% of the crystal assemblage in Redondo Creek (Table 1). In all the Valle Grande rhyolites (excluding the obsidian from Cerro Del Medio), sanidine, quartz, and anorthoclase make up 85–98% of the crystal assemblage (Table 1). In Banco Bonito, plagioclase and quartz account for 58% of the crystals present (Table 1). The rhyolite from Banco Bonito contains the highest abundance of mafic phases including Fe-Ti oxides, biotite, hornblende, and clinopyroxene (Table 1). The rhyolite from Banco Bonito contains two distinct varieties of crystalline clots: (1) partially melted biotite-granitoid composed of plagioclase + biotite + quartz + hornblende + melt ± sanidine, where plagioclase crystals in the clot exhibit similar textures to plagioclase crystals found in Banco Bonito (Supplementary Material 3 Figure S2); and (2) a spinel-gabbro with plagioclase + clinopyroxene + Fe-Ti oxides (Supplementary Material 3 Figure S2). Both of these clot types are found throughout the Banco Bonito sample but are not observed in any other post-collapse rhyolite in our study.

4.2 Whole rock major and trace element geochemistry

The post-collapse rhyolites range from LSR to HSR (73.9–77.3 wt% SiO_2 ; Table 2). We follow the LSR to HSR nomenclature of Gardner et al. [1986], which distinguishes HSR from LSR on the basis of their whole rock compositions. The HSRs have >76 wt% SiO_2 , 0.4–0.12 wt% MgO, <0.63 wt% CaO,

 \leq 27 ppm Sr, and \leq 125 ppm Ba and the LSRs have <76 wt% SiO₂, >0.21 wt% MgO, >0.87 wt% CaO, 107–197 ppm Sr, and 431–961 ppm Ba (Table 2). The full suites of whole rock major and trace element abundances for each sample are available in Supplementary Material 2 Table S2. The HSRs (Cerro Del Medio, Cerro Del Abrigo, Cerro Santa Rosa, Cerro San Luis, Cerro Seco, and South Mountain) all show similarities in whole rock composition with little to no variation in concentrations of SiO₂, Al₂O₃, or FeO^T (Table 2). The LSRs (Redondo Creek, San Antonio, and Banco Bonito) have some variation in their silica content (73.9–75.6 wt% SiO₂) but but are similar in their elevated concentrations of Al₂O₃ and CaO (Table 2).

4.3 Glasses

In the HSRs, average analyses of groundmass glasses normalized to 100 wt%, have little variation in major element abundances (Table 3 and Supplementary Material 2 Table S3). The LSRs with glass analyses (San Antonio and Banco Bonito) contain more Al₂O₃ and CaO, compared to the HSRs (Table 3). The anorthite number (An#; defined in footnote 5 in Table 3) is a method of describing a glass composition in terms of its plagioclase-forming components [Carmichael et al. 1977; Lange et al. 2009] and is similar to the ratio $X_{\text{Ca}}/(X_{\text{Ca}}+X_{\text{Na}})$ in a glass composition. The An#s in glasses from the HSRs range from 2.05-2.90 and those from the LSRs range from 4.31–4.76 (Table 3). Average halogen contents in glasses from the post-collapse rhyolites have a total range from 0.08-0.29 wt% F and 0.06-0.16 wt% Cl, both Cerro San Luis (0.28 wt% F and 0.16 wt% Cl) and Cerro Seco (0.29 wt% F and 0.16 wt% Cl) have the highest average halogen contents.

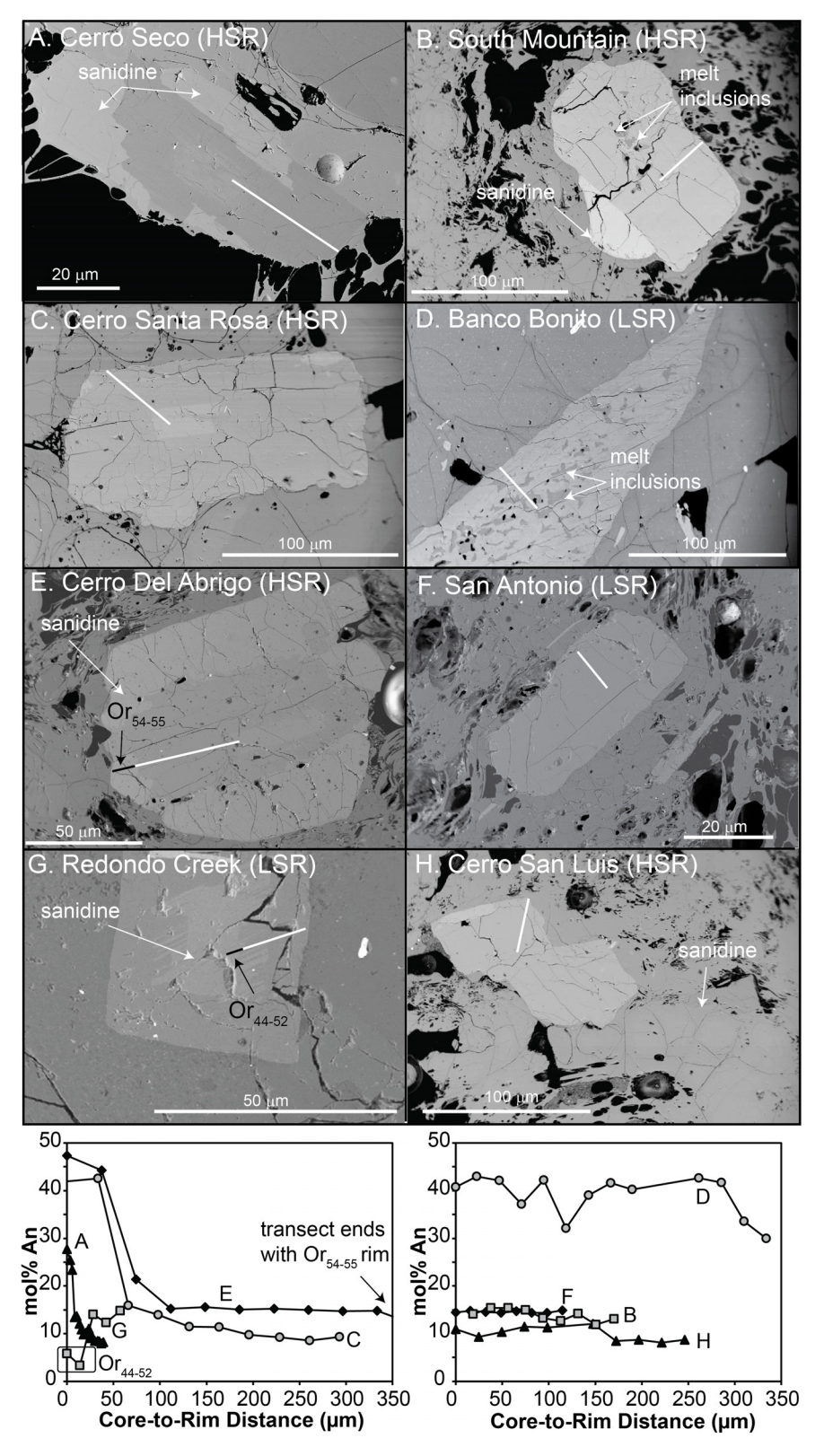


Figure 2: Backscatter electron (BSE) images of representative anorthoclase and plagioclase textures are shown. Crystals with inclusions of other minerals in their cores are shown in the left column; homogenous crystals and those with melt inclusions are shown in the right column (grey scale has been adjusted to better show anorthoclase/plagioclase phenocrysts relative to the glass or groundmass). Microprobe transects to determine mol% An (core to rim) are shown as white lines, and compositions are shown in the bottom plots as a function of distance along the traverse. Calcic cores are more commonly seen [A, C, E] but an instance of a sanidine core was found in Redondo Creek [G]. Black transect lines or boxes indicate orthoclase (and refer to mol% Or on transect plots). Trace melt inclusions are found in South Mountain [B]; and Banco Bonito is primarily composed of plagioclase with sieved cores and faceted rims [D]. However, the majority of anorthoclase phenocrysts are homogeneous.

Table 2: Sample locations and whole rock major and trace element analyses.

Dome* Sample Type [†]	RC NMVC-45,82 LSR	CM CM_1C HSR	CA NMVC_63 HSR	CSR CSR_1C HSR	CSL CSL_1 HSR	CS CS_1B HSR	SA NMVC_66 LSR	SM SM_1A HSR	BB BB_1A LSR			
Lat.	35.87774	35.92579	35.94994	35.95253	35.94368	35.95318	35.93274	35.82411	35.83225			
Long.	-106.57432	-106.44695	-106.49507	-106.49669	-106.53115	-106.58739	-106.60723	-106.53226	-106.59214			
SiO ₂	75.6	77.1	77.1	77.2	77.0	77.3	73.9	76.5	74.1			
TiO_2	0.34	0.09	0.09	0.11	0.08	0.08	0.24	0.13	0.29			
Al_2O_3	13.6	12.5	13.1	12.5	12.8	12.5	13.9	12.9	13.4			
FeO^T	0.87	1.04	0.78	0.94	0.87	0.82	1.71	0.99	1.89			
MnO	0.02	0.06	0.06	0.06	0.08	0.08	0.06	0.06	0.06			
MgO	0.21	0.05	0.05	0.08	0.04	0.04	0.51	0.12	0.63			
CaO	0.87	0.38	0.42	0.45	0.41	0.41	1.23	0.63	1.76			
Na ₂ O	3.93	4.15	3.64	4.00	3.99	4.02	3.83	3.84	3.72			
K_2O	4.53	4.59	4.75	4.55	4.70	4.78	4.56	4.83	4.06			
P_2O_5	0.04	0.02	0.02	0.06	< 0.01	0.01	0.06	0.02	0.09			
LOI‡	0.61	0.62	2.6	1.97	2.38	2.99	2.24	1.77	0.68			
Total	99.2	98.5	101	99.9	99.9	100	100	101	101			
Trace element analyses (ppm)												
Rb	103	163	190	184	253	283	136	216	136			
Sr	137	4.00	12.0	8.00	3.00	4.00	107	27.0	197			
Zr	313	141	98	113	112	108	168	110	131			
Ba	961	28	65	39	19	22	431	125	556			
Rare ear	rth element and	alyses (ppm)										
La	55.0	50.8	35.5	36.0	28.7	36.5	41.0	38.4	34.3			
Ce	102	98.4	71.3	70.9	62.1	77.5	77.9	76.2	61.0			
Y	22.0	37.0	44.0	43.0	63.0	62.0	33.0	45.0	22.0			
Sc	2.00	2.00	1.00	3.00	2.00	2.00	4.00	3.00	4.00			
Pr	10.3	10.7	7.54	7.76	7.07	8.59	8.19	8.23	6.07			
Nd	34.0	35.9	24.9	26.3	24.3	30.0	26.9	28.5	20.2			
Sm	5.80	7.40	5.70	6.10	6.50	7.70	5.20	6.30	3.80			
Eu	0.79	0.22	0.19	0.2	0.08	0.08	0.43	0.23	0.51			
Gd	4.30	6.20	5.10	5.40	6.40	7.30	4.30	6.00	3.00			
Tb	0.70	1.10	1.00	1.00	1.40	1.50	0.80	1.10	0.50			
Dy	4.10	7.20	6.90	6.80	9.50	10.6	5.10	7.80	3.30			
Но	0.80	1.50	1.50	1.40	2.10	2.30	1.10	1.60	0.70			
Er	2.30	4.30	4.50	4.50	6.60	7.30	3.30	5.00	2.30			
Tm	0.35	0.66	0.70	0.68	1.05	1.16	0.52	0.81	0.37			
Yb	2.30	4.60	4.90	4.80	7.40	8.10	3.60	5.70	2.80			
Lu	0.37	0.71	0.77	0.74	1.16	1.26	0.55	0.90	0.46			

^{*}See Table 1 for dome abbreviations. †Type of rhyolite, either low-silica rhyolite (LSR) or high-silica rhyolite (HSR). ‡LOI – loss on ignition.

4.4 Anorthoclase and plagioclase

We selected a subset of anorthoclase (defined as feldspar with An_{8-20} and Or_{9-25}) and plagioclase (defined as feldspar with $>An_{20}$ and $<Or_{8}$) for microprobe analysis in each sample (Table 4), except from the obsidian Cerro Del Medio (where microlites proved too small to analyze) that represented the textural and compositional diversity observed in the thin sections and BSE imaging (Figure 2 and Supplementary Material 3 Figures S3–S5). The majority of anorthoclase in all our samples except Banco Bonito are compositionally homogeneous (i.e. unzoned), subhedral to eu-

hedral, tabular to blocky, and range in size from 250 µm to as large as 3 mm (Figure 2 and Supplementary Material 3 Figures S3–S4). Banco Bonito contains sieved plagioclase instead of anorthoclase (Figure 2D, Figure 3H, and Supplementary Material 3 Figure S5). Anorthoclase in some samples (Cerro Del Abrigo, Cerro Seco, Cerro San Luis, and South Mountain) often have sanidine crystals on their margins, either appearing as rims (Figure 2A and E) or a sanidine growing on a single side of the anorthoclase (Supplementary Material 3 Figures S3–S4). In rhyolites from Cerro Del Abrigo, Cerro Santa Rosa, and Cerro Seco, a very low abundance (i.e.

Dome* Type [†] n^{\ddagger}	CM HSR 6	1σ	CA HSR 10	1σ	CSR HSR 5	1σ	CSL HSR 6	1σ	CS HSR 6	1σ	SA LSR 10	1σ	SM HSR 6	1σ	BB LSR 6	1σ
SiO ₂	76.8	0.26	77.3	0.11	77.2	0.49	76.8	0.10	77.0	0.11	76.3	0.37	77.2	0.20	76.3	0.29
TiO_2	0.10	0.20	0.08	0.11	0.09	0.43	0.09	0.10	0.05	0.02	0.15	0.05	0.08	0.20	0.21	0.23
Al_2O_3	12.7	0.02	12.3	0.07	12.4	0.11	12.4	0.06	12.5	0.10	12.9	0.20	12.4	0.14	13.2	0.19
FeO ^T	0.83	0.11	0.78	0.03	0.79	0.06	0.83	0.04	0.82	0.03	0.88	0.07	0.70	0.04	0.69	0.07
MnO	0.04	0.02	0.07	0.03	0.07	0.03	0.09	0.03	0.10	0.04	0.04	0.02	0.08	0.02	0.04	0.02
MgO	0.04	0.01	0.04	0.01	0.03	0.02	0.03	0.02	0.02	0.02	0.09	0.02	0.05	0.01	0.11	0.03
CaO	0.33	0.02	0.38	0.01	0.40	0.02	0.37	0.02	0.37	0.02	0.66	0.06	0.46	0.03	0.73	0.01
Na ₂ O	4.25	0.06	3.92	0.03	4.63	1.06	4.27	0.05	4.22	0.07	3.78	0.07	3.92	0.05	3.84	0.09
K ₂ O	4.67	0.04	4.79	0.05	4.09	1.53	4.62	0.05	4.53	0.05	4.90	0.07	4.87	0.06	4.75	0.07
P_2O_5	0.01	0.02	0.01	0.02	0.01	0.01	0.00	0.02	0.00	0.02	0.02	0.02	0.00	0.02	0.03	0.02
F	0.14	0.03	0.16	0.02	0.17	0.02	0.28	0.02	0.29	0.03	0.14	0.03	0.13	0.01	0.08	0.02
Cl	0.12	0.01	0.16	0.01	0.14	0.01	0.16	0.01	0.16	0.01	0.10	0.01	0.10	0.02	0.06	0.01
Total [§]	100	0.16	96.7	0.32	100	0.28	96.9	0.46	96.8	0.26	97.6	0.42	97.5	1.08	99.6	0.39
An#	2.05	0.10	2.40	0.07	2.33	0.26	2.26	0.11	2.28	0.12	4.31	0.42	2.90	0.17	4.76	0.07
Mg#¶	10.2	1.23	10.6	5.17	8.24	5.62	7.50	5.58	5.15	5.25	19.5	6.24	14.3	5.10	30.1	10.1
Fe ³⁺ /Fe ^{T 7}	0.14	0.01	0.13	0.01	0.15	0.00	0.13	0.00	0.12	0.01	0.14	0.00	0.15	0.01	0.21	0.01
Fe ²⁺ /Mg ⁸	8.82	0.11	8.38	0.10	10.9	0.02	12.0	0.04	18.0	0.21	4.12	0.01	5.80	0.08	2.32	0.04

Table 3: Analyses of matrix glass normalized to 100 wt%.

See Table 1 for dome abbreviations. † Type of rhyolite, either low-silica rhyolite (LSR) or high-silica rhyolite (HSR). $^{\ddagger}n$ – number of analyses. Average total for microprobe glass analyses. $^{||}$ An# = $100X_{An}/(X_{An}+X_{Ab})$, where $X_{An}=64.0(X_{Ca0})(X_{Al_2O_3})(X_{SiO_2})^2$ and $X_{Ab}=18.963(X_{Na_2O})^{0.5}(X_{Al_2O_3})^{0.5}(X_{SiO_2})^{\ddagger}$ [Lange et al. 2009]. ¶ Mg# = 100Mg/(Mg+Fe²⁺) in mole fraction, standard deviation in Mg# calculated by propagating the highest FeO^T and lowest MgO (and lowest FeO^T and highest MgO) to show the full range in Mg#. $^{}\sigma$ standard deviation for Fe³⁺/Fe^T is calculated through using the maximum and minimum temperature and fO_2 values, based on σ deviation, in the model of Kress and Carmichael [1991] to determine molar Fe³⁺ and Fe²⁺ for the standard deviation range of conditions. $^{\diamond}\sigma$ standard deviation for Fe²⁺/Mg is calculated through using the maximum and minimum temperature and fO_2 values, based on σ deviation, in the model of Kress and Carmichael [1991].

two or three crystals per thin section) of anorthoclase crystals contain small (10–20 µm) anorthite-rich cores in their interiors (Figure 2A, C, and E). The anorthite-rich cores either appear skeletal and have a sharp compositional gradient to the crystal rim (e.g. Figure 2C) or the cores have diffuse margins with compositions that gradually decrease in An-content to the rim compositions (Figure 2A). A small percentage of anorthoclase in the rhyolite from South Mountain contain melt inclusions (Figure 2B). Most plagioclase crystals in Banco Bonito have sieved cores with homogeneous, thick (≥20 µm) rims (Figure 2D and Supplementary Material 3 Figure S5). The rhyolite from Redondo Creek is the only sample in this study to contain anorthoclase crystals with a sanidine cores (Figure 2G), anorthoclase with sanidine rims are also commonly found in this Redondo Creek sample (Supplementary Material 3 Figure S3).

Anorthoclase compositions (Table 4) in the Valles Grande Member range from anorthoclase to oligoclase (An_{9-20} ; Figure 3). Samples from Cerro San Luis and Cerro Seco have a narrow range in anorthoclase composition, and primarily contain homogeneous crystals (Figure 2F and Figure 3). The anorthite-rich cores found in anorthoclase in HSRs Cerro Del Abrigo, Cerro Santa Rosa, and Cerro Seco (Figure 2A, C, and Figure 3) are oligoclase-andesine (An_{20-45}) and do not form a continuum with anorthoclase compositions (Fig-

ure 3). Rhyolites from San Antonio and South Mountain contain anorthoclase crystals with a wider range in anorthite content (anorthoclase-oligoclase An_{8–22}; Figure 3F–G). The rhyolite from Banco Bonito contains homogeneous, unzoned plagioclase crystals and sieved plagioclase cores that have thick homogeneous rims (Figure 3H and Supplementary Material 3 Figure S5). The compositions of sieved cores range from oligoclase-andesine An_{20–46} (Figure 3H, hachure pattern), homogeneous rims and unzoned crystals range from oligoclase-andesine An_{22–34} (Figure 3H, gray pattern). Anorthoclase and plagioclase crystals in Redondo Creek range from anorthoclase-oligoclase An_{12–26} (Figure 3A). Though we highlight the range of textures that occur in each sample, we emphasize that the majority of anorthoclase crystals in all rhyolites except Banco Bonito have minimal zoning and are commonly euhedral (Supplementary Material 3 Figures S3-S5). Sample Banco Bonito is the only sample that commonly features plagioclase with sieve textures and homogeneous rims. We report the average anorthoclase or plagioclase rim compositions measured in each sample (i.e. the average composition of anorthoclase or plagioclase in contact with the glass) in Table 4; all analyses of anorthoclase and plagioclase, including An-rich plagioclase in cores, can be found in Supplementary Material 2 Table S4 and their corresponding BSE images are in Supplementary Material 3 Figures S3–S5.

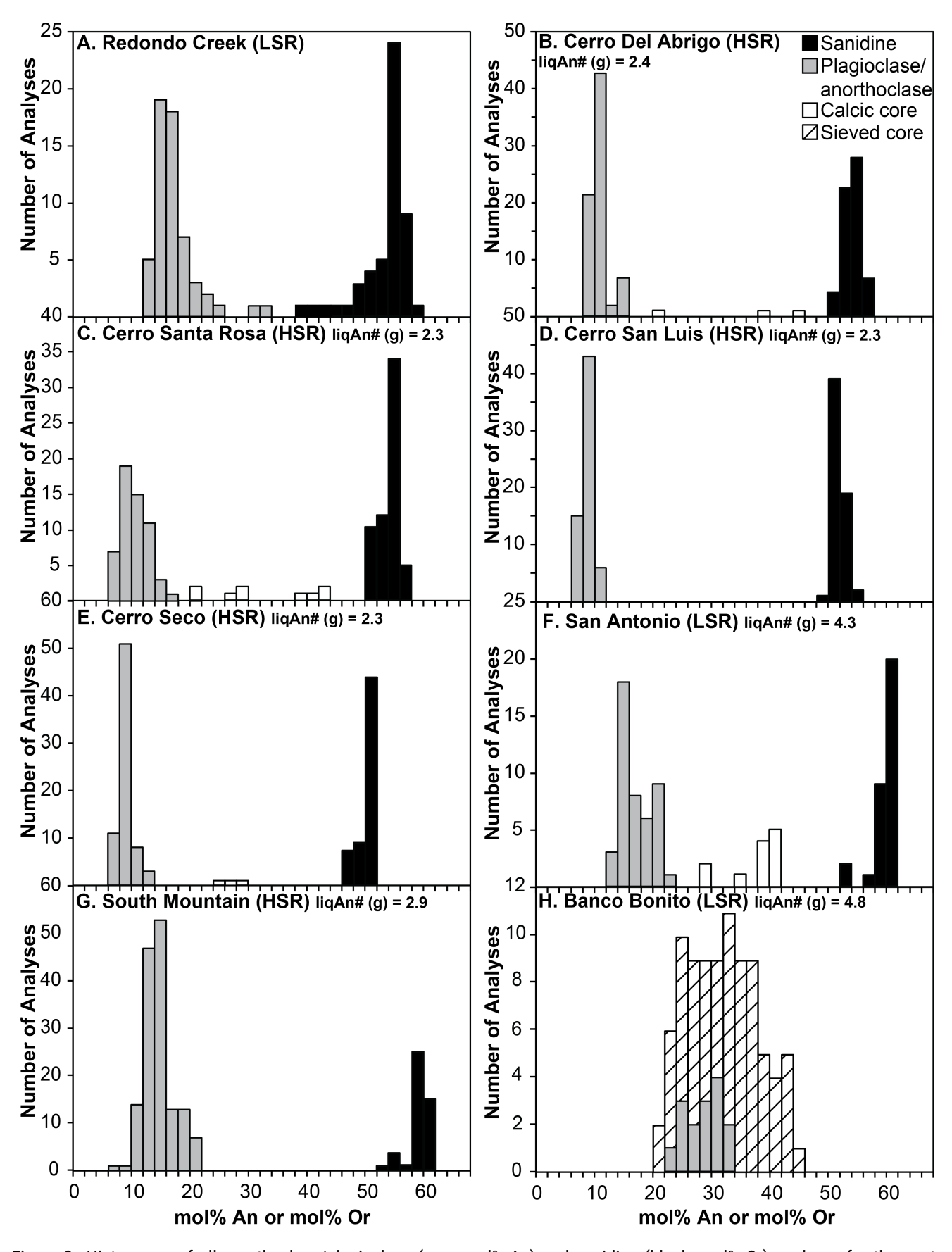


Figure 3: Histograms of all anorthoclase/plagioclase (grey, mol% An) and sanidine (black, mol% Or) analyses for the post-collapse rhyolites. Trace anorthoclase crystals with calcic cores are shown in white, and sieved plagioclase cores are shown with a hachure pattern (mol% An, see text for discussion). LiqAn# (g) = glass An#, see Table 3 for definition and calculation of An#.

RC CA **CSR CSL** CS 2σ 2σ Dome* 2σ 2σ 2σ 2σ 2σ SA SM 2σ BB n^{\dagger} 9 8 7 6 7 7 12 8 SiO₂ 64.1 1.39 65.5 1.45 64.8 1.11 66.1 0.92 66.3 0.70 64.1 2.11 64.5 5.10 63.3 4.21 Al_2O_3 21.8 2.03 21.2 1.44 20.6 0.40 20.4 0.36 21.1 0.36 21.6 1.18 21.0 3.55 22.9 2.72 FeO^T 0.22 0.09 0.12 0.05 0.15 0.08 0.17 0.07 0.190.06 0.18 0.06 0.15 0.21 0.19 0.05 MnO 0.00 0.02 0.00 0.02 0.01 0.03 0.00 0.01 0.03 0.03 0.01 0.02 0.01 0.04 0.01 0.02 MgO 0.00 0.03 0.00 0.01 0.00 0.06 0.01 0.02 0.00 0.02 0.01 0.02 0.00 0.03 0.01 0.01 0.29 CaO 2.98 1.84 1.86 0.39 1.65 0.57 1.75 0.13 2.68 1.25 1.69 1.24 4.44 1.54 1.65 9.33 9.37 8.98 0.90 6.75 1.93 8.16 Na₂O 8.52 1.82 0.19 9.07 0.48 0.26 9.59 0.13 0.54 K_2O 3.61 0.29 1.95 0.39 1.73 0.24 0.35 0.13 5.38 1.20 2.11 1.87 1.83 1.53 1.07 0.46 Total 99.7 1.33 99.9 1.27 98.1 2.02 99.6 1.45 101 0.77 99.0 2.65 99.4 1.94 100 0.34 Cation normalization on the basis of δ oxygens Si 2.88 80.0 2.90 0.06 2.91 0.01 2.93 0.01 2.91 0.02 2.86 0.05 2.90 0.18 2.80 0.16 0.01 0.02 Al (IV) 1.15 0.00 1.10 1.09 0.02 1.07 1.09 1.14 0.05 1.11 0.20 1.19 0.15 0.07 Fe^{3+} (IV) 0.01 0.10 0.00 0.01 0.00 0.01 0.00 0.01 0.00 0.01 0.00 0.01 0.01 0.01 0.00 0.00 Mn 0.00 0.00 0.00 0.00 0.00 0.00 0.00 0.00 0.00 0.00 0.00 0.00 0.00 0.00 0.00 0.00 Mg 0.00 0.00 0.00 0.000.00 0.00 0.000.00 0.00 0.00 0.00 0.00 0.00 0.00 0.00 0.00 Ca 0.14 0.00 0.09 0.02 0.08 0.03 80.0 0.01 0.08 0.01 0.13 0.06 0.08 0.06 0.21 80.0 0.79 Na 0.74 0.09 0.80 0.01 0.00 0.00 0.00 0.82 0.01 0.78 0.07 0.59 0.00 0.70 0.00 0.03 К 0.02 0.01 0.02 0.09 0.14 0.07 0.12 0.15 0.11 0.11 0.80 0.10 0.01 0.17 0.05 5.04 0.04 5.00 0.02 4.98 0.02 0.01 5.00 0.01 5.00 0.02 4.83 0.22 4.98 0.09 No. cations 0.10 9 2.4 22 An (mol%) 14 8.6 1.8 8 8 8.0 8 1.4 13 6.1 10 5.6 6.0 Ab (mol%) 74 14 80 0.7 81 0.6 82 0.4 82 0.7 78 6.7 73 4.2 71 3.3 Or (mol%) 12 22 1.7 11 2.3 10 10 1.9 9 8.0 17 6.3 7 3.2 11 1.1 H_2O^{Ox} (wt%)[‡] 5.2 4.9 5.0 4.8 5.4 4.6 5.4 $P_{\text{H}_2\text{O}}^{\text{Ox}} \text{(MPa)}^{\$}$ 142 149 130 165 124 165 139 H₂O^{Hbld} (wt%)|| 5.1 6.0 5.8 5.9 5.6 5.0 3.7 $P_{\rm H_2O}^{\rm Hbld} \, (\rm MPa)^{\P}$ 178 148 184 187 194 142 86 H_2O^{CPX} (wt%)* 3.6 4.6 $P_{\rm H_2O}^{\rm CPX} \, ({\rm MPa})^{\diamond}$

Table 4: Analyses of anorthoclase and plagioclase rims with H₂O contents from plagioclase-hygrometry.

*See Table 1 for dome abbreviations. $\dagger n$ – number of analyses. \ddagger Calculated from plagioclase hygrometry using Fe-Ti oxide temperature [Ghiorso and Evans 2008] and glass composition. §Calculated at Fe-Ti oxide temperature, using the volatile solubility model of Ghiorso and Gualda [2015] in lacovino et al. [2021]. || Calculated from plagioclase hygrometry using hornblende temperature [Putirka 2016] and glass composition. ¶Calculated at hornblende temperature, using the volatile solubility model of Ghiorso and Gualda [2015] in lacovino et al. [2021]. *Calculated from plagioclase hygrometry using clinopyroxene temperature [Putirka 2008] and glass composition. Calculated at clinopyroxene temperature, using the volatile solubility model of Ghiorso and Gualda [2015] in lacovino et al. [2021].

Sanidine 4.5

We selected sanidine crystals from Redondo Creek, Cerro Del Abrigo, Cerro Santa Rosa, Cerro San Luis, Cerro Seco, San Antonio, and South Mountain that represented the textural and compositional diversity observed in thin section and with BSE imaging for each post-collapse rhyolite (Table 5). Sanidine crystals in the post-collapse rhyolites are typically 250 µm to 2 mm in size, blocky, unzoned, and subhedral to euhedral (Figure 4 and Supplementary Material 3 Figures S6– S7). The majority of sanidine crystals are compositionally homogeneous, but some (i.e. ≤15% of all sanidine crystals) feature mineral inclusions (e.g. quartz and anorthoclase; Figure 4C and E) or melt inclusions (Figure 4B and D). There is no apparent correlation between sanidine composition and the

presence of melt inclusions, with individual crystals showing <5 mol% variation in orthoclase (Figures 3 and 4 and Table 5). In the Valle Grande rhyolites, Cerro Del Abrigo, Cerro Santa Rosa, Cerro San Luis, Cerro Seco, San Antonio, and South Mountain (Figure 3B–G and Figure 4B–F), there is little variation in sanidine composition and orthoclase content typically varies ≤10 mol% for any individual rhyolite (Figures 3 and 4 and Table 5). Redondo Creek again is notable in that it contains sanidine crystals with oligoclase cores (e.g. Figure 4A) and the widest range of orthoclase (Or₃₉₋₅₉; Figure 3A) in the post-collapse rhyolites. All sanidine analyses are provided in Supplementary Material 2 Table S5 and accompanying BSE images are in Supplementary Material 3 Figures S6–S7.

82

124

Table 5: Analyses of sanidine rims.

Dome*	RC	2σ	CA	2σ	CSR	2σ	CSL	2σ	CS	2σ	SA	2σ	SM	2σ
n^{\dagger}	8		8		5		5		7		6		4	
SiO ₂	66.3	2.10	65.3	1.05	64.5	1.56	67.0	0.57	66.5	0.58	68.1	1.09	64.4	2.92
Al_2O_3	17.9	1.22	19.4	1.79	18.6	0.25	18.9	0.27	19.4	0.28	17.1	0.54	18.3	0.82
${ m FeO^T}$	0.16	0.02	0.14	0.04	0.15	0.03	0.12	0.02	0.10	0.02	0.23	0.09	0.12	0.02
MnO	0.00	0.02	0.00	0.02	0.00	0.02	0.03	0.01	0.01	0.03	0.00	0.03	0.03	0.03
MgO	0.00	0.02	0.00	0.02	0.00	0.00	0.00	0.02	0.00	0.01	0.02	0.02	0.00	0.00
CaO	0.28	0.10	0.26	0.09	0.19	0.02	0.32	0.05	0.24	0.04	0.34	0.11	0.20	0.04
Na ₂ O	4.41	0.63	4.93	0.65	4.95	0.28	5.61	0.19	5.30	0.17	4.70	0.64	4.30	0.31
K_2O	9.83	1.00	9.94	1.21	9.76	0.40	8.63	0.17	8.90	0.23	8.43	1.51	10.6	0.87
Total	98.9	2.47	100	1.74	98.2	1.59	100	0.65	101	0.80	99.0	0.51	98.0	4.57
Cation norm	alizati	on on t	the bas	is of 8 (oxygens	3								
Si	3.03	0.05	2.96	0.07	2.98	0.02	3.00	0.01	2.98	0.01	3.08	0.03	2.99	0.02
Al (IV)	0.96	1.01	1.04	0.09	1.01	0.02	1.00	0.01	1.02	0.01	0.91	0.03	1.00	0.01
Fe ³⁺ (IV)	0.01	1.07	0.01	0.00	0.01	0.00	0.00	0.00	0.00	0.00	0.01	0.00	0.00	0.00
Mn	0.00	0.01	0.00	0.00	0.00	0.00	0.00	0.00	0.00	0.00	0.00	0.00	0.00	0.00
Mg	0.00	0.00	0.00	0.00	0.00	0.00	0.00	0.00	0.00	0.00	0.00	0.00	0.00	0.00
Ca	0.01	0.02	0.01	0.00	0.01	0.00	0.02	0.00	0.01	0.00	0.02	0.01	0.01	0.00
Na	0.39	0.43	0.43	0.06	0.44	0.02	0.49	0.02	0.46	0.01	0.41	0.06	0.39	0.01
K	0.57	80.0	0.57	0.07	0.57	0.03	0.49	0.01	0.51	0.01	0.49	0.09	0.63	0.04
No. cations	4.97	0.03	5.02	0.04	5.02	0.02	4.99	0.01	4.99	0.00	4.91	0.05	5.02	0.03
An (mol%)	1	0.5	1	0.4	1	0.1	1	0.2	1	0.2	2	0.6	1	0.3
Ab (mol%)	40	5.5	42	6.3	43	2.3	49	1.2	47	1.3	45	6.7	38	1.5
Or (mol%)	59	5.6	57	6.2	56	2.5	50	1.3	52	1.5	53	7.3	61	1.8

^{*}See Table 1 for dome abbreviations. $^{\dagger}n$ – number of analyses.

4.6 Fe-Ti oxides

We analyzed titanomagnetite-ilmenite pairs and individual crystals, avoiding crystals that exhibited exsolution lamellae or oxidation. Titanomagnetites range in size from 25–200 µm, and ilmenites typically range in size between 20–50 µm, though we observed a few magnetite crystals that were larger (\sim 75 µm) in the HSR from Santa Rosa. Ilmenite and titanomagnetite crystals are anhedral to subhedral and range in habit from rounded to blocky. Titanomagnetite and ilmenite compositions have a narrow range in composition in individual samples, spanning <2.13 mol% ulvospinel for 7 analyses and \leq 1.63 mol% ilmenite out of 10 analyses, respectively (Table 6); all analyses are provided in Supplementary Material 2 Table S6.

4.7 Mafic silicates

We observed biotite phenocrysts in all of the post-collapse rhyolites, the obsidian Cerro Del Medio contains small (<10 μm) biotite crystals in the groundmass that were too minute to analyze. We targeted biotite grains large enough to yield reasonable analyses (i.e. crystals >10 μm that did not show significant separation between crystallographic planes). Biotite crystal textures range from euhedral and tabular to subhedral, with intergrown Fe-Ti oxides found in all textures (Figure 5A and C). Biotites range in size from 25–1000 μm , Cerro Santa Rosa contains the full range of biotite crystal size,

while all other samples have biotite that ranges from 25–500 µm. The Mg#s for biotites range from 46.7 to 66.2, where Mg#= $100X_{\rm MgO}/(X_{\rm FeO}+X_{\rm MgO})$, when all iron (i.e. Fe^T = Fe³⁺ + Fe²⁺) is calculated as ferrous iron (Table 7); there is no correlation between biotite texture, size, or composition. We use the model of Li et al. [2020] to determine the Fe³⁺/Fe^T in biotites from the post-collapse rhyolites (0.29–0.34; Table 7) to determine Mg#, based on ferrous iron only. When Mg# of biotites are re-calculated on the basis of ferrous iron only, they increase to 54.6–74.7 (Table 7); all biotite analyses are provided in Supplementary Material 2 Table S7.

We analyzed hornblende crystals in each sample, where hornblende abundance varied from trace abundances (i.e. two to three crystals per thin section in the HSRs, as in Cerro San Luis) to ≥1% of the mode in the Banco Bonito (Supplementary Material 3 Figure 1I). We selected hornblende crystals for analysis that were as representative as possible throughout each sample, based on appearance under petrographic microscopes and BSE imaging. For the rhyolites that contained limited hornblende (i.e. Redondo Creek, Cerro San Luis, and San Antonio; Table 8), we assume the hornblendes we analyzed have representative compositions for our thin sections but note there may be greater variation in the natural sample. Hornblendes range from euhedral and faceted with diamond-shapes (Figure 5B and H), to subhedral and blocky (Figure 5D). Hornblende crystals are typically 25–50 µm, though

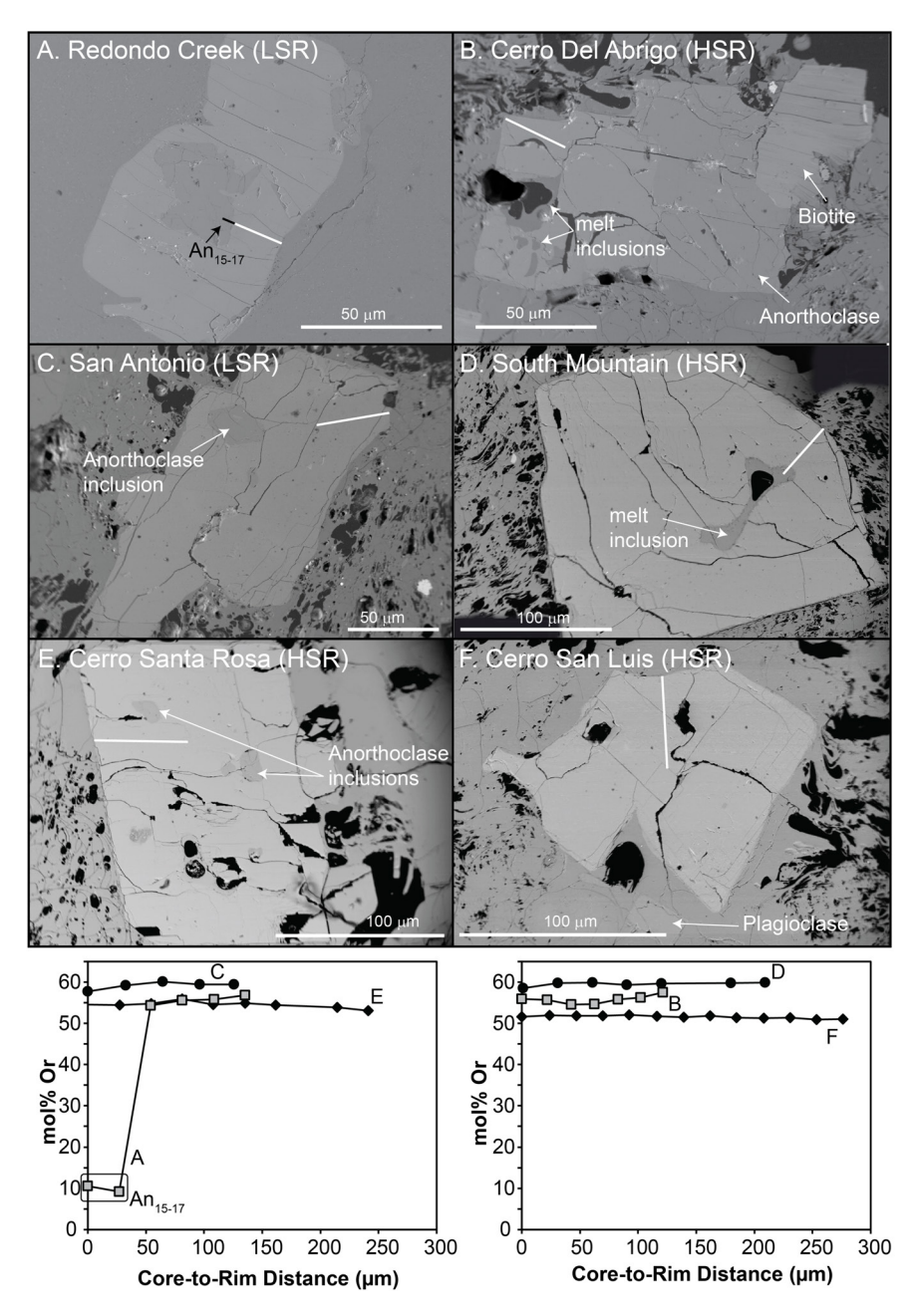


Figure 4: Backscatter electron images of representative sanidine textures found in the rhyolites are shown (grey scale has been adjusted to better show sanidine phenocrysts relative to the glass or groundmass). Microprobe transects to determine mol% Or (core to rim) are shown as white lines and compositions are shown in the bottom plots as a function of distance along the traverse. Sections of the traverses that correspond to anorthoclase (i.e. Redondo Creek [A], San Antonio [C], and Cerro Santa Rosa [E]) are shown in black and noted with a box in the traverse. Melt inclusions are found in San Antonio [B] and South Mountain [D]. The majority of the sanidine crystals in all samples are homogeneous (e.g. Cerro San Luis [F]).

trace hornblende that exceed 400 µm are found in Cerro Del Abrigo, Cerro Seco, San Antonio, and Banco Bonito (Figure 5D and H). Hornblende Mg#s from all the rhyolites range from 44.3 to 68.7, when all iron is considered to be ferrous (Table 8) and there is no correlation between Mg#s and crystal sizes; all analyses are provided in Supplementary Material 2 Table S8. The Fe³⁺/Fe^T in hornblendes in the post-caldera rhyolites is between 0.08–0.10 for all samples (Table 8) based on stoichiometric calculations using the model of Putirka [2016]. The Mg#s in hornblendes increase slightly and range from 46.8 to 70.6 (Table 8), when calculated on the basis of ferrous

iron only instead of total iron. Hornblende in all the samples, except Banco Bonito, span a narrow range in $X_{\rm Al}$, $X_{\rm Ti}$, and $X_{\rm Na}$ on the basis of 23 oxygen (Supplementary Material 3 Figure S8). Hornblende in Banco Bonito is heterogeneous with respect to $X_{\rm Al}$, $X_{\rm Ti}$, and $X_{\rm Na}$ and has two to three times the variation seen the other rhyolites (Supplementary Material 3 Figure S8).

The LSRs from Redondo Creek, San Antonio, and Banco Bonito contained trace pyroxenes (Table 1), which were analyzed when they were observed (Table 9); all pyroxene analyses are provided in Supplementary Material 3 Table S9.

Table 6: Average magnetite-ilmenite pair analyses, temperatures, and oxygen fugacities.

Dome*	RC	2σ	CM	2σ	CA	2σ	CSR	2σ	CSL	2σ	CS	2σ	SA	2σ	SM	2σ	BB	2σ
Ilmenite																		
n^{\dagger}	2		4		5		1		3		2		1		4		10	
SiO ₂	0.07	0.04	0.03	0.03	0.05	0.04	0.27	-	0.06	0.05	0.02	0.00	0.21	-	0.06	0.04	0.04	0.04
TiO_2	44.7	0.31	45.8	0.47	45.6	0.49	44.7	-	45.2	0.15	45.4	0.03	45.7	-	45.0	0.49	38.4	0.86
Al_2O_3	0.12	0.06	0.02	0.02	0.05	0.03	0.04	-	0.04	0.02	0.03	0.03	0.15	-	0.06	0.03	0.25	0.20
Fe_2O_3	14.2	0.57	11.9	0.68	12.1	0.68	14.5	-	12.3	0.25	11.3	0.14	11.9	-	13.3	0.51	27.7	1.55
FeO	37.4	0.58	38.3	0.72	36.0	0.39	35.6	-	35.2	0.29	35.2	0.14	36.2	-	35.9	0.71	30.5	1.22
Cr_2O_3	0.00	0.00	0.00	0.00	0.00	0.01	0.00	-	0.01	0.03	0.01	0.01	0.01	-	0.00	0.01	0.01	0.05
MnO	1.37	0.00	2.27	0.23	3.85	0.40	3.62	-	4.79	0.18	4.90	80.0	1.83	-	3.51	0.13	1.03	0.15
MgO	0.95	0.11	0.60	0.05	0.93	0.05	0.92	-	0.59	0.05	0.58	0.03	2.71	-	0.94	0.05	1.91	0.25
CaO	0.03	0.00	0.03	0.03	0.10	0.07	0.24	-	0.01	0.02	0.03	0.01	0.03	-	0.01	0.05	0.03	0.05
Total	98.7	0.11	99.0	0.32	98.6	0.58	99.9	-	98.2	0.61	97.6	0.08	98.7	-	98.7	0.68	99.9	0.47
$X_{\rm ilm}$	81.3	0.82	82.4	1.31	78.0	0.65	76.4	-	76.4	0.13	77.0	0.23	78.7	-	77.6	0.88	67.0	1.63
Magnetite	2																	
n^{\dagger}	2		5		3		6		5		7		4		3		6	
SiO ₂	0.09	0.02	0.09	0.05	0.09	0.06	0.11	0.06	0.11	0.04	0.10	0.03	0.10	0.04	0.09	0.02	0.07	0.04
TiO_2	7.26	0.72	9.02	0.58	8.55	0.44	7.72	0.15	8.82	0.09	8.43	0.76	8.30	0.19	7.26	0.72	5.93	0.41
Al_2O_3	0.86	0.01	0.78	0.05	0.73	0.07	0.70	0.05	0.65	0.04	0.66	0.10	1.34	0.11	0.86	0.01	1.44	0.09
Fe_2O_3	52.7	1.25	50.8	1.31	51.1	0.94	54.0	0.56	50.0	0.41	50.5	1.34	50.8	0.27	52.7	1.25	55.5	1.73
FeO	35.2	0.58	38.0	0.31	36.3	0.54	36.5	0.33	36.4	0.23	35.6	1.21	36.3	0.34	35.2	0.58	33.7	0.27
Cr_2O_3	0.02	0.03	0.00	0.02	0.01	0.01	0.01	0.01	0.00	0.00	0.01	0.04	0.03	0.01	0.02	0.03	0.05	0.07
MnO	1.59	0.16	1.23	0.19	1.84	0.11	1.56	0.04	2.16	0.05	2.50	0.53	0.81	0.04	1.59	0.16	0.87	0.05
MgO	0.39	0.01	0.34	0.05	0.49	0.02	0.35	0.02	0.24	0.05	0.21	0.12	1.08	0.11	0.39	0.01	1.18	0.09
CaO	0.02	0.03	0.00	0.02	0.03	0.01	0.05	0.06	0.00	0.01	0.01	0.02	0.04	0.03	0.02	0.03	0.03	0.03
Total	98.2	0.13	100	0.29	99.4	0.21	101	0.55	98.4	0.57	98.0	0.59	99.2	0.36	98.2	0.13	98.8	1.44
$X_{ m ulv}$	27.2	0.78	25.6	1.68	24.5	1.28	21.8	0.46	25.6	0.23	24.6	2.13	23.6	0.47	21.1	2.06	17.0	1.36
<i>T</i> (°C) [‡]	824	12	772	23	763	14	764	4	771	3	750	19	782	5	746	19	790	19
ΔNNO [‡]	0.4	0.0	0.2	0.1	0.1	0.1	0.4	0.0	0.0	0.0	-0.1	0.1	0.3	0.0	0.4	0.1	1.3	0.1

*See Table 1 for dome abbreviations. $^{\dagger}n$ – number of analyses. ‡ Temperature and Δ NNO are average ($\pm 2\sigma$) from all possible pairings of ilmenite and magnetite analyses using the model of Ghiorso and Evans [2008].

Both clinopyroxenes and orthopyroxenes are typically 20–100 µm. Orthopyroxenes are primarily anhedral in shape in Redondo Creek, while in San Antonio and Banco Bonito both orthopyroxenes and clinopyroxenes range from anhedral (Figure 5G) to euhedral and elongate (Figure 5E). The orthopyroxene Mg#s range from 59.7–71.3, when all iron is calculated as ferrous. We estimate the orthopyroxenes have Fe^{3+}/Fe^{T} that ranges from 0.03–0.06 based on the method of Droop [1987]. Clinopyroxenes in San Antonio and Banco Bonito vary from Mg# 62.9 to 72.7 when all iron is calculated as ferrous. The Fe^{3+}/Fe^{T} in the clinopyroxenes range from 0.03–0.12 when applying the method of Droop [1987], and clinopyroxene Mg#s increase to 69.1 in San Antonio and 74.5 in Banco Bonito when calculated using ferrous iron only (Table 9).

5 Discussion

Our objective in this study is to determine the changes to the storage conditions (temperature, oxygen fugacity, H_2O contents, and pressure) that occurred following the voluminous eruption of the UBT in the post-caldera rhyolites

at Valles Caldera by applying established model thermometers [e.g. Ghiorso and Evans 2008; Putirka 2008; 2016], hygrometers [Waters and Lange 2015], and barometers [Mutch et al. 2016; Iacovino et al. 2021] to minerals and glass compositions. However, before we can apply these models, we first evaluate if the minerals in the rhyolites are in textural and chemical equilibrium and, therefore, represent the magmatic storage conditions. In general, the rhyolites are crystal-rich (13.3–28.5 vol% crystals), and so we discount the use of whole-rock compositions as representative liquid compositions in the event that a sample has a large xenocrystic load that could alter a whole rock composition. Instead, we utilize the compositions of matrix glass and mineral rims to evaluate mineral-melt equilibrium (Figure 6).

The first step to evaluating mineral-melt equilibrium in the rhyolites requires an initial evaluation of Fe-Ti oxide equilibrium, then solving for their temperatures and oxygen fugacities, and finally evaluating Fe-Mg equilibrium in mafic silicates. The temperatures and fO_2 values recorded by Fe-Ti oxides in each sample are required to determine the melt Fe²⁺

Table 7: Average biotite compositions, Mg#s, and Fe-MgKD values.

Dome*	RC	2σ	CA	2σ	CSR	2σ	CSL	2σ	CS	2σ	SA	2σ	SM	2σ	BB	2σ
n^\dagger	23		8		4		4		2		9		13		5	
SiO ₂	37.5	1.19	38.0	0.81	37.1	2.16	37.5	1.38	41.1	1.50	37.6	0.50	37.0	0.84	37.9	0.33
TiO_2	5.03	0.42	3.83	0.23	4.08	0.42	3.23	0.31	2.73	0.45	4.05	0.16	3.92	0.17	4.84	0.38
Al_2O_3	13.0	0.55	12.6	1.28	12.9	0.43	12.8	2.10	13.9	2.69	12.8	0.34	12.7	0.60	13.6	0.33
FeO^T	18.5	1.09	20.0	1.12	20.7	1.45	20.4	2.37	17.6	1.81	21.2	0.43	19.9	0.81	14.3	0.36
MnO	0.28	0.06	0.60	80.0	0.62	0.11	0.84	0.14	0.60	0.11	0.56	0.04	0.62	0.05	0.20	0.03
MgO	12.6	0.59	11.6	1.26	11.4	0.56	9.82	0.96	8.28	0.98	11.5	0.31	11.5	0.68	15.7	0.35
CaO	0.02	0.02	0.07	0.09	0.04	0.06	0.05	0.05	0.44	0.11	0.02	0.03	0.04	0.03	0.05	0.06
Na ₂ O	0.62	0.05	0.51	0.17	0.48	0.11	0.46	0.13	0.18	0.01	0.44	0.03	0.55	0.05	0.73	0.06
K_2O	8.82	0.23	8.54	1.20	8.54	0.41	8.07	0.87	5.15	1.30	8.99	0.30	8.92	0.31	8.76	0.27
F	1.06	0.65	1.46	0.13	1.35	0.13	1.93	0.27	1.58	0.06	1.29	0.08	1.63	0.30	0.87	0.56
Cl	0.12	0.03	0.18	0.03	0.19	0.06	0.17	0.02	0.14	0.03	0.17	0.01	0.17	0.02	0.09	0.02
Total	97.6	1.53	97.3	2.40	100	0.82	98.0	1.37	93.0	0.33	98.6	0.71	97.0	1.38	97.0	0.67
$\mathrm{Fe^{3+}/Fe^{T\ddagger}}$	0.29	0.04	0.33	0.06	0.33	0.02	0.30	0.06	0.33	0.03	0.31	0.01	0.31	0.02	0.34	0.06
Cations calculated using Li et al. [2020]																
Si (IV)	2.87	0.05	2.92	0.06	2.87	0.08	2.94	0.13	3.12	0.27	2.89	0.16	2.88	0.04	2.86	0.04
Al (IV)	0.94	0.08	0.81	0.14	0.86	0.06	0.80	0.10	0.72	0.12	0.84	0.07	0.87	0.05	1.03	0.17
Fe ³⁺ (VI)	0.19	0.06	0.26	0.10	0.27	0.03	0.26	0.07	0.16	0.15	0.27	0.10	0.25	0.03	0.11	0.13
Al (VI)	0.24	0.08	0.33	0.11	0.31	0.03	0.38	0.15	0.52	0.24	0.31	0.17	0.30	0.03	0.17	0.11
Mg (VI)	1.47	0.06	1.38	0.15	1.38	0.07	1.23	0.20	0.91	0.48	1.36	0.35	1.40	0.07	1.77	0.29
Fe^{2+} (VI)	0.84	0.09	0.85	0.07	0.89	0.05	0.94	0.05	0.75	0.28	0.93	0.14	0.91	0.08	0.60	0.29
Fe ³⁺ (VI)	0.16	0.05	0.17	0.03	0.18	0.03	0.14	0.07	0.20	0.06	0.16	0.05	0.14	0.03	0.19	0.08
Ti (VI)	0.28	0.05	0.22	0.06	0.23	0.02	0.20	0.05	0.18	0.02	0.23	0.04	0.23	0.01	0.27	0.04
Mn (VI)	0.02	0.01	0.04	0.02	0.04	0.01	0.06	0.01	0.04	0.03	0.04	0.00	0.04	0.00	0.01	0.02
К	0.83	0.02	0.81	80.0	0.81	0.04	0.80	0.06	0.59	0.29	0.84	0.19	0.85	0.03	0.82	0.04
Na	0.09	0.03	0.08	0.03	0.07	0.02	0.07	0.02	0.03	0.08	0.07	0.03	0.08	0.01	0.11	0.02
Ca	0.00	0.00	0.01	0.01	0.00	0.00	0.00	0.00	0.04	0.04	0.00	0.02	0.00	0.00	0.00	0.00
Calculated 1	using a	ll iron	as ferr	ous iro	n											
$^{\mathrm{Fe/Mg}}X$ -tal §	0.80	0.10	0.93	0.09	0.94	0.08	1.07	0.06	1.14	0.15	1.03	0.19	0.93	0.08	0.51	0.02
Mg#	55.4	3.37	51.9	2.41	51.6	2.00	48.2	1.42	46.7	3.23	49.4	4.21	51.9	2.21	66.2	1.1
Fe/MgKD			0.11	0.01	80.0	0.01	0.09	0.01	0.06	0.01	0.25	0.04	0.16	0.01	0.22	0.01
Calculated 1	using fe	errous i	iron on	ıly												
Fe/MgX-tal§	0.57	0.05	0.62	80.0	0.65	0.05	0.76	0.05	0.83	0.12	0.68	0.04	0.65	0.40	0.34	0.01
Mø#	63.7	2.18	61.8	2.95	60.7	1.93	56.7	1.59	54.6	3.66	59.5	1.23	60.6	3.05	74.7	0.47
Fe/MgK _D	00	0	0.07	0.01	0.06	0.00	0.06	0.00	0.04	0.01	0.17	0.01	0.11	0.07	0.15	0.00
			0.0.	0.01	0.00	0.00	0.00	0.00	0.01	0.01	0.1.	0.01	0.11	0.0.	0.10	

^{*}See Table 1 for dome abbreviations. $^{\dagger}n$ – number of analyses. $^{\ddagger}Fe^{3+}/Fe^{T}$, Fe^{2+} , and Fe^{3+} calculated using the machine learning approach of Li et al. [2020]. $^{\$}Fe/Mg$ X-tal is the ratio of Fe/Mg in the crystal, the same is true in the following tables.

content in the expression for the Fe²⁺-Mg exchange constant (Fe-Mg K_D) between the ratio of $X_{\rm Fe^{2+}}$ to $X_{\rm Mg}$ in mafic minerals [$(X_{\rm Fe^{2+}}/X_{\rm Mg})^{\rm minerals}$] and the ratio of $X_{\rm Fe^{2+}}$ to $X_{\rm Mg}$ in the melt [$(X_{\rm Fe^{2+}}/X_{\rm Mg})^{\rm melt}$]:

$$^{\text{Fe-Mg}}\text{K}_{\text{D}} = \frac{(X_{\text{Fe}^{2+}}/X_{\text{Mg}})^{\text{mineral}}}{(X_{\text{Fe}^{2+}}/X_{\text{Mg}})^{\text{melt}}}$$
 (1)

We incorporate the temperature and values of fO_2 From Fe-Ti oxide geothermobarometry [Ghiorso and Evans 2008] and the matrix glass compositions (Table 3) into the empirically calibrated model of Kress and Carmichael [1991], which determines Fe³⁺/Fe²⁺, Fe²⁺/Mg, and Mg# in silicate melts. We

use the melt Fe²⁺/Mg values to calculate the Fe-MgK_D between mafic silicate minerals and melt (Equation 1). An assumption inherent to utilizing the oxygen fugacity derived from Fe-Ti oxides in the calculation of the Fe-MgK_D values is that the Fe-Ti oxides provide accurate records of both the temperature and fO_2 at the time the mafic silicates crystallized.

Following assessment of equilibrium for each silicate mineral, we apply models from the literature to the mineral compositions to determine the pre-eruptive conditions recorded by each phase. We compare our results to the storage conditions of the UBT to understand how magmatism changed following the last caldera-forming eruption.

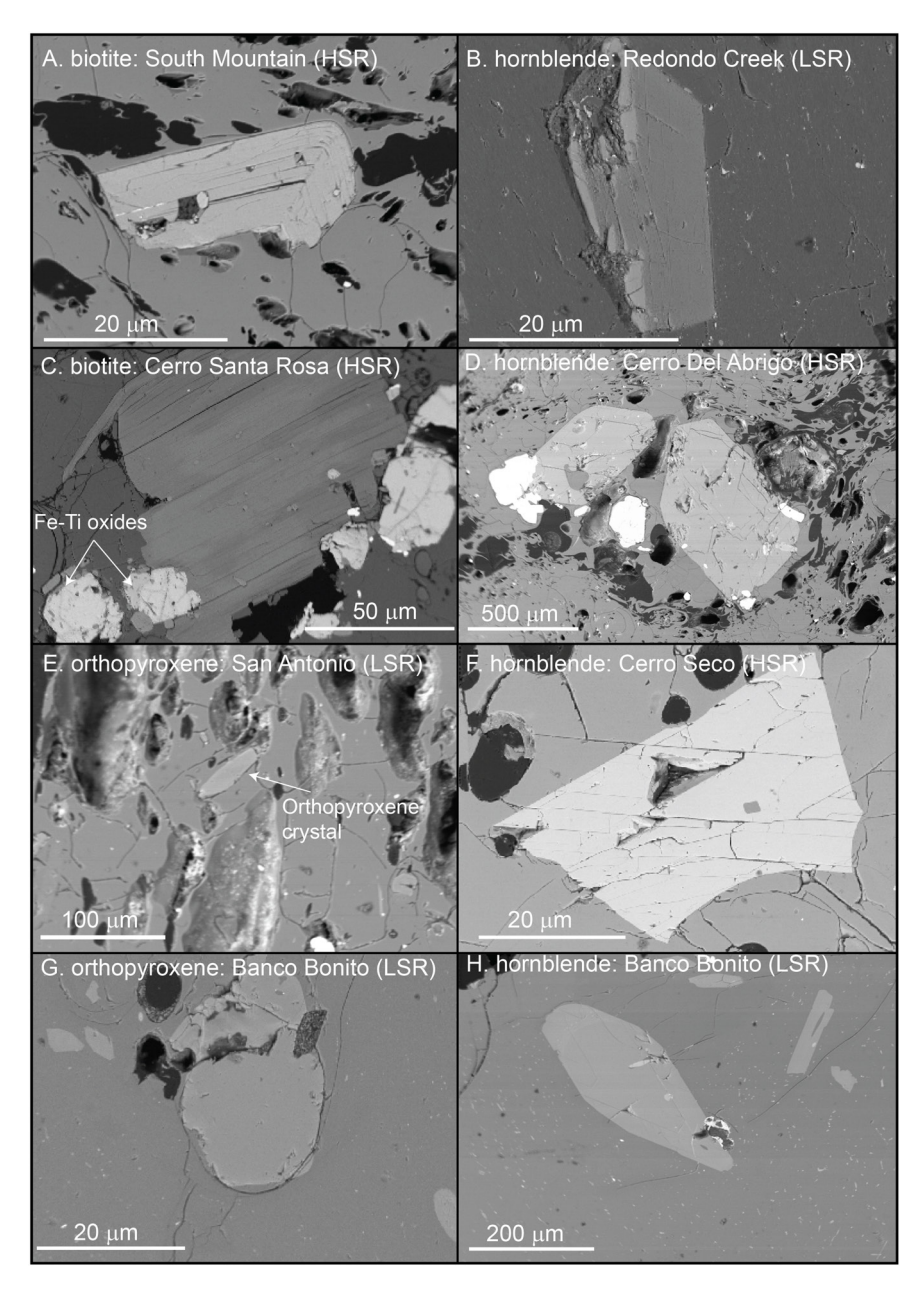


Figure 5: Backscatter electron images of biotite, hornblende, and orthopyroxene phenocrysts are shown to represent textures across the samples. Biotites typically range in size from medium laths ([A] South Mountain), to slightly larger crystals (>50 μ m) ([C] Cerro Santa Rosa) intergrown with magngetite-ilmenite pairs. Hornblendes are typically small <50 μ m and faceted ([B] Redondo Creek and [F] Cerro Seco), but occasional larger >400 μ m crystals are present as well ([D] Cerro Del Abrigo and [H] Banco Bonito). Orthopyroxene crystals are typically small, elongate, and euhedral ([E] San Antonio), or small and anhedral ([G] Banco Bonito).

5.1 Fe-Ti oxides: equilibrium tests, geothermobarometry, and calculation of glass Mg#s

We use the Mg-Mn equilibrium exchange between titanomagnetite and ilmenite criteria of Bacon and Hirschmann [1988] to exclude pairs of ilmenite and titanomagnetite that are not in equilibrium with each other. We calculate temperatures and oxygen fugacity by incorporating pairings of titanomagnetite-ilmenite compositions in each sample (Table 6) that pass the Bacon and Hirschmann [1988] equilibrium test (Supplementary Material 3 Figure S9) into the two

Fe-Ti oxide geothermometer and oxygen barometer models of Ghiorso and Evans [2008]. Temperatures ($\pm 2\sigma$, where the standard deviation reflects the range of crystal compositions; Table 6) range from 746 \pm 19 °C to 824 \pm 12 °C (Table 6 and Figure 7A). Oxygen fugacity, reported as ΔNNO , ranges from -0.1 \pm 0.1 to +1.3 \pm 0.1 (Table 6). The reported $\pm 2\sigma$ values for Fe³⁺/Fe^T, Fe²⁺/Mg, and Mg# reported in Table 3 are determined by propagating the average and $\pm 2\sigma$ range of temperatures and fO_2 values recorded by Fe-Ti oxides through the model of Kress and Carmichael [1991].

Table 8: Average hornblende compositions, Mg#, Fe-Mg KD values, temperatures, and pressures.

Dome*	RC	2σ	CA	2σ	CSR	2σ	CSL	2σ	CS	2σ	SA	2σ	SM	2σ	BB	2σ
n^{\dagger}	4		16		7		4		22		2		12		30	
SiO_2	48.1	1.04	47.6	0.98	46.1	2.36	45.4	0.86	45.8	0.92	46.1	0.40	46.5	1.67	47.0	3.10
TiO_2	1.27	0.05	1.13	0.14	1.03	0.09	1.07	0.08	1.06	0.13	1.08	0.06	1.26	0.25	1.60	0.66
Al_2O_3	5.48	0.31	5.42	0.36	5.57	0.34	5.82	0.48	5.70	0.64	5.77	0.37	6.11	0.50	7.62	2.49
FeO^T	15.7	0.42	16.6	1.78	19.4	2.29	20.9	0.76	21.1	0.87	18.9	0.37	18.3	1.35	12.4	1.37
MnO	0.69	0.03	1.14	0.29	1.70	0.53	1.90	0.09	1.97	0.14	1.49	0.10	1.22	0.13	0.49	0.25
MgO	13.9	0.63	12.6	1.11	10.8	2.33	9.30	0.18	9.46	0.54	11.5	0.24	11.3	0.76	15.3	1.40
CaO	10.6	0.29	10.7	0.25	10.0	0.72	9.84	0.36	9.79	0.20	9.97	0.01	10.6	0.33	11.2	0.46
Na ₂ O	1.59	0.03	1.74	0.07	1.93	0.27	2.03	0.11	2.01	0.10	1.71	0.08	1.84	0.17	1.71	0.45
K ₂ O	0.55	0.03	0.59	0.07	0.68	0.11	0.73	0.11	0.70	0.13	0.68	0.04	0.69	0.07	0.64	0.23
F	0.59	0.03	0.93	0.06	1.16	0.75	1.14	0.07	1.15	0.08	0.78	0.04	1.01	0.19	0.50	0.10
Cl	0.08	0.02	0.08	0.02	0.11	0.01	0.12	0.02	0.12	0.03	0.10	0.01	0.09	0.01	0.04	0.02
Total	98.6	1.50	98.6	0.72	98.6	1.49	98.2	1.01	98.9	0.81	98.1	0.71	98.8	0.75	98.5	0.92
Cations calcul	lated ı	ısing <mark>P</mark>	utirka	[2016]	1											
Si (IV)	7.09	0.10	7.12	0.08	7.05	0.09	7.02	0.08	7.04	0.11	7.02	0.09	7.02	0.14	6.85	0.38
Al (IV)	0.91	0.10	0.88	0.08	0.95	0.09	0.98	0.08	0.96	0.11	0.98	0.09	0.98	0.13	1.15	0.38
Al(VI)	0.08	0.04	0.08	0.05	0.05	0.03	0.09	0.06	0.08	0.05	0.06	0.03	0.11	0.08	0.17	0.16
Fe ³⁺ (VI)	0.18	0.01	0.20	0.02	0.24	0.04	0.27	0.02	0.27	0.02	0.23	0.00	0.22	0.02	0.13	0.02
Ti (VI)	0.14	0.01	0.13	0.02	0.12	0.01	0.12	0.01	0.12	0.02	0.12	0.01	0.13	0.09	0.18	0.07
Mg (VI)	3.04	0.12	2.81	0.23	2.46	0.43	2.15	0.05	2.17	0.12	2.62	0.04	2.54	0.14	3.34	0.28
Fe ²⁺ (VI)	1.56	0.08	1.78	0.22	2.13	0.39	2.38	0.09	2.36	0.10	1.97	0.02	2.00	0.21	1.19	0.19
Fe^{2+} (excess)	0.22	0.03	0.11	0.02	0.12	0.06	0.06	0.02	0.08	0.03	0.20	0.06	0.08	0.03	0.20	0.09
Mn (excess)	0.09	0.00	0.14	0.04	0.22	80.0	0.25	0.01	0.26	0.02	0.19	0.01	0.16	0.02	0.06	0.03
Ca	1.69	0.02	1.71	0.04	1.64	0.06	1.63	0.05	1.61	0.04	1.61	0.05	1.71	0.05	1.73	80.0
Na	0.01	0.01	0.04	0.04	0.02	0.04	0.06	0.05	0.05	0.04	0.01	0.00	0.05	0.04	0.01	0.11
Fe ³⁺ /Fe ^T	0.09	0.01	0.10	0.00	0.10	0.01	0.10	0.00	0.10	0.01	0.09	0.00	0.10	0.00	0.08	0.01
Calculated us	ing all	iron o	ıs ferre	ous iro	n											
Fe/MgX-tal	0.64	0.05	0.74	0.15	1.02	0.33	1.26	0.07	1.13	0.10	0.92	0.00	0.91	0.13	0.46	0.08
Mø#	60.9	2.02	57.5	4.76	49.7	8.27	44.3	1.29	44.4	2.17	52.1	0.03	52.4	3.38	68.7	3.88
Fe/MgK _D			0.09	0.03	0.09	0.04	0.10	0.03	0.06	0.01	0.22	0.04	0.15	0.05	0.20	0.07
Calculated us	ing fer	rous ii	on on	ly												
Fe/MgX-tal	0.34	0.03	0.67	0.13	0.92	0.30	1.13	0.06	1.25	0.11	0.83	0.00	0.82	0.11	0.42	0.08
Mg#	63.2	2.12	59.9	4.71	52.3	8.28	46.8	1.28	47.0	2.21	54.6	0.05	54.9	3.39	70.6	3.82
Fe/MgK _D			0.08	0.02	0.08	0.03	0.09	0.00	0.07	0.01	0.20	0.00	0.14	0.02	0.18	0.03
T (°C) [‡]			757	15	744	9	738	14	733	20	748	12	761	16	835	67
P (MPa)§	179	31	173	16	183	22	196	17	191	26	154	70	203	22	271	127

^{*}See Table 1 for dome abbreviations. $^{\dagger}n$ – number of analyses. ‡ Temperature calculated using the Putirka [2016] model.

5.2 Equilibrium tests for silicates

We use the average Mg#s and Fe $^{2+}$ /Mg ratios from the glasses (Table 3) and the $X_{\rm Fe}^{2+}/X_{\rm Mg}$ for biotites, hornblendes, and pyroxenes determined by incorporating our mineral analyses into stoichiometric models in the literature [Droop 1987; Putirka 2008; 2016; Li et al. 2020, Tables 7, 8 and 9] to calculate the Fe-MgKD values for the mafic silicates. Though Fe-MgKD values typically provide a reasonable estimate of mineral phase equilibrium, propagation of standard deviations of vanishingly small MgO contents measured in glasses via

microprobe (Table 3) can result in a large range of Fe^{2+}/Mg ratios, and, as a result, can lead to large variations in $^{Fe-Mg}K_D$ values associated with a given mineral Fe^{2+}/Mg . We carry out the calculations of the $^{Fe-Mg}K_D$ values for mafic silicates (presented in Tables 7, 8 and 9) but note that the large errors are a consequence of the low MgO contents (and associated errors) in glasses in the natural samples, rendering this test of equilibrium only somewhat useful, compared to its application in mafic liquids. We consider the crystals to be in equilibrium

[§]Pressure calculated using the Mutch et al. [2016] model.

Table 9: Average pyroxene compositions, Mg#, Fe-MgKD values, and temperatures.

Dome* Phase n^{\dagger}	RC Opx 1	2σ	SA Opx 9	2σ	SA Cpx 3	2σ	BB Opx 12	2σ	BB Cpx 2	2σ
SiO ₂	51.0	-	53.6	1.55	48.7	1.93	53.8	1.06	53.5	0.78
TiO_2	0.28	-	0.24	0.16	0.82	0.31	0.17	0.09	0.19	0.01
Al_2O_3	1.11	-	2.11	1.43	4.27	0.55	1.06	1.31	0.56	0.25
FeO^T	24.7	-	16.5	8.36	11.1	4.56	18.7	3.50	9.25	1.20
MnO	1.37	-	0.46	0.49	0.31	0.14	0.93	0.77	0.50	0.01
MgO	20.4	-	25.9	4.95	14.0	3.48	25.0	3.04	15.1	0.16
CaO	1.18	-	1.72	1.10	18.7	0.45	1.10	0.38	20.9	1.00
Na ₂ O	0.04	-	0.03	0.04	0.46	0.31	0.00	0.08	0.32	0.06
K_2O	0.00	-	0.02	0.02	0.07	0.07	0.00	0.03	0.00	0.00
Total	100	-	101	1.10	98.5	1.04	101	1.82	100	0.14
Cations cal	culated	using	Putirk	a [2008	3]					
Si	1.94	-	1.94	0.04	1.86	0.04	1.94	0.04	1.99	0.01
Al (IV)	0.06	-	0.06	0.04	0.14	0.04	0.06	0.04	0.01	0.01
Al (VI)	0.00	-	0.03	0.03	0.05	0.01	0.01	0.02	0.01	0.01
$Fe^{3+}(VI)$	0.09	-	0.03	0.05	0.12	0.09	0.06	0.06	0.02	0.03
Ti (VI)	0.01	-	0.01	0.00	0.02	0.01	0.01	0.00	0.01	0.00
Mg (VI)	1.16	-	1.41	0.25	0.80	0.18	1.41	0.13	0.84	0.01
Fe^{2+} (VI)	0.69	-	0.45	0.29	0.24	0.15	0.46	0.11	0.26	0.03
Mn	0.04	-	0.01	0.02	0.01	0.00	0.02	0.02	0.02	0.00
Ca	0.05	-	0.07	0.04	0.76	0.03	0.05	0.01	0.83	0.03
Na	0.00	-	0.00	0.00	0.03	0.02	0.00	0.01	0.02	0.00
K	0.00	-	0.00	0.00	0.00	0.00	0.00	0.00	0.00	0.00
Total	4.04	-	4.01	0.02	4.04	0.03	4.02	0.02	4.01	0.02
Fe ³⁺ /Fe ^T	0.05	-	0.03	0.04	0.12	0.09	0.06	0.05	0.03	0.04
Calculated	using a	ll iror	ı as fer	rous ire	on					
Fe/MgX-tal	0.67	-	0.41	0.24	0.61	0.41	0.37	0.12	0.38	0.09
Mg#	59.7	-	71.3	11.9	62.9	17.4	70.6	5.03	72.7	4.79
Fe/MgKD	-	-	0.10	0.05	0.15	0.09	0.16	0.05	0.16	0.03
Calculated	using fe	errous	iron o	nly						
Fe/MgX-tal	0.59	_	0.37	0.25	0.46	0.28	0.42	0.10	0.34	0.04
Mσ#	62.7	-	73.7	13.5	69.1	13.9	72.9	6.10	74.5	2.28
Fe/MgKD	_	_	0.09	0.02	0.11	0.03	0.18	0.04	0.15	0.01
T (°C) [‡]					823	10			799	5
(- /										

^{*}See Table 1 for dome abbreviations. $^{\dagger}n$ – number of analyses. ‡ Temperature calculated using the Putirka [2008] model (eq. 33 from their study) and average H₂O contents, based on the average Fe-Ti oxide and hornblende temperatures (Tables 6 and 8 and Figure 7A).

with the glasses when the Mg#s and $^{\text{Fe-Mg}}K_D$ values of mafic silicates and glasses overlap with experimental results.

Biotites from the post-collapse rhyolites have Mg#s from 54.6–74.7 and $^{\rm Fe-Mg}{\rm K}_{\rm D}$ values of 0.05–0.17 (Table 7), which overlap with the experimental dataset in which biotites have Mg#s that range from 27–88 and $^{\rm Fe-Mg}{\rm K}_{\rm D}$ values of 0.05–0.30 [Supplementary Material 3 Figure S10; Icenhower and London 1995; Righter and Carmichael 1996; Lukkari and Holtz 2007; Mutch et al. 2016].

Hornblendes from the post-collapse rhyolites have Mg#s from 46.8–70.6 and $^{\rm Fe\text{-}Mg}\rm K_D$ values of 0.06–0.20, and over-

lap in Mg# with crystals grown in experiments [Sato 2005; Tomiya et al. 2010; Mutch et al. 2016] that have Mg#s that range from 35–78 and $^{\rm Fe-Mg}{\rm K}_{\rm D}$ values of 0.09–0.40 (Figure 6A). Hornblende in the rhyolite from Banco Bonito have variations in Ti, Al, and Na between analyses that are not detectable in BSE (Figure 5 and Supplementary Material 3 Figure S8). There is no consistent variation in Ti, Al, and Na contents with size. For example, hornblende microlites are typically assumed to grow during late-stage crystallization from the melt; however, the aggregate set of electron microprobe analyses on microlites show they have compositions that re-

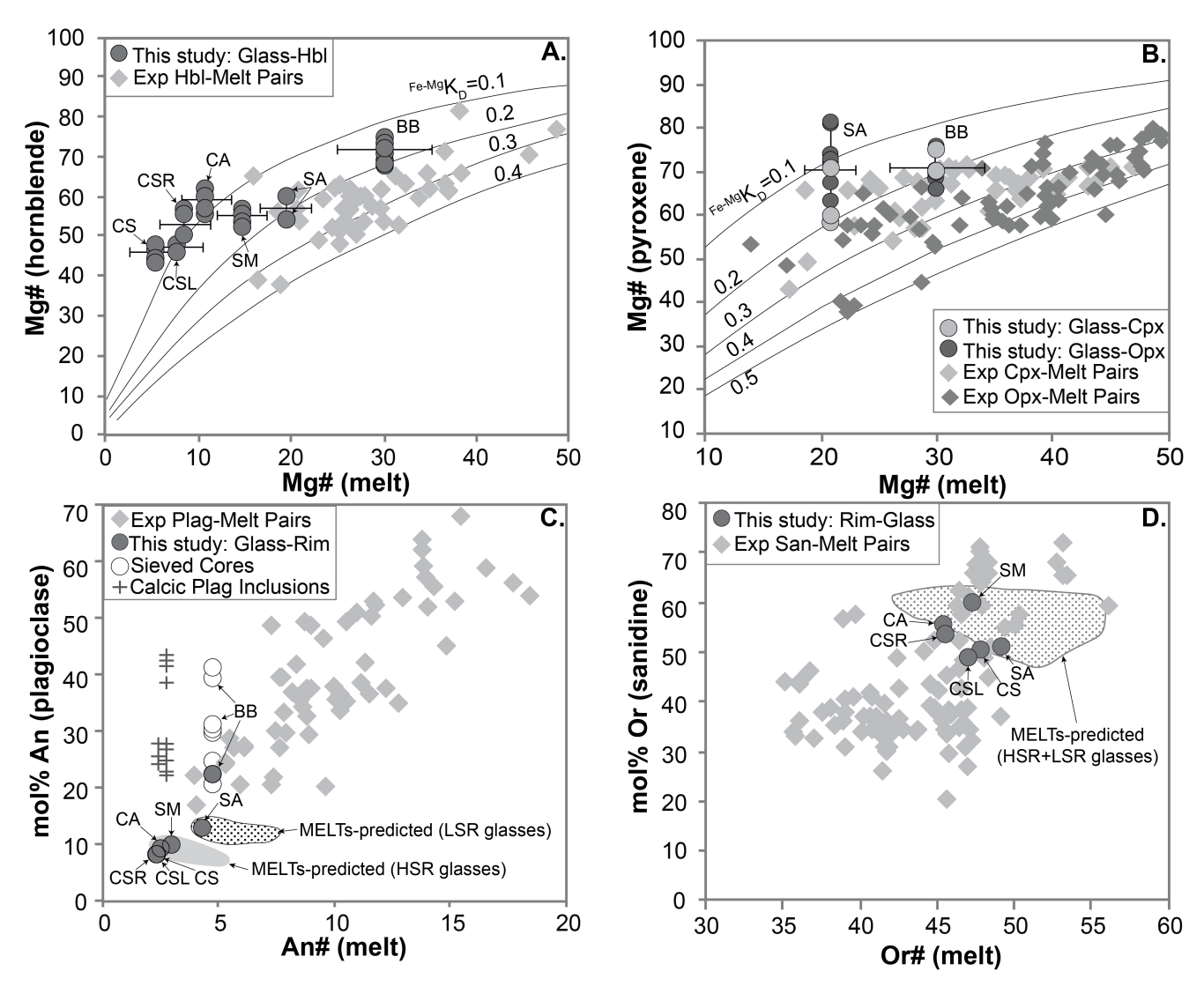
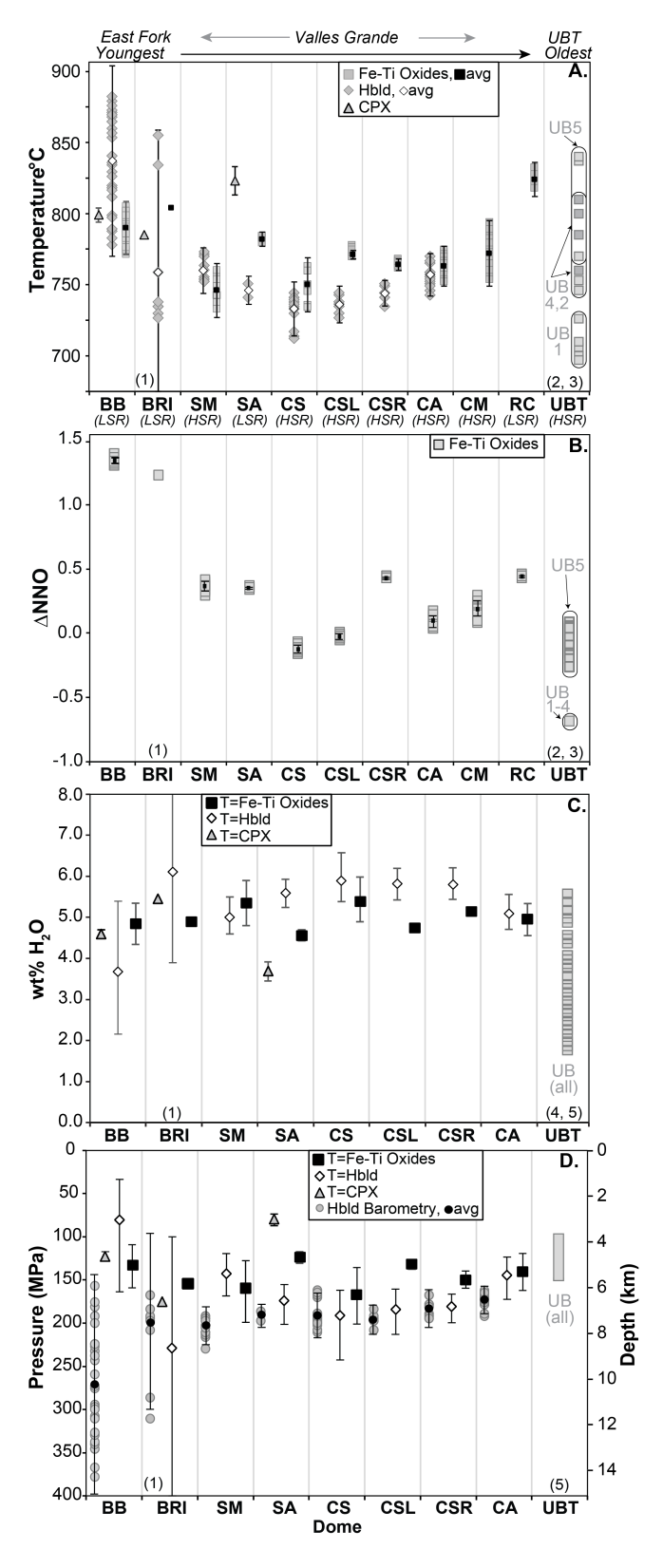


Figure 6: Mg# in the melt shown relative to Mg# in [A] hornblende and [B] pyroxenes. Contours of Fe-MgKD values are shown as a function of melt and crystal Mg#. Error bars for Mg# in the melt are calculated by propagating the entire range of Fe-Ti oxide temperatures and oxygen fugacities with the range of MgO and FeO^T measured in glass analyses through the model of Kress and Carmichael [1991] to obtain the largest possible range of Mg#. Experimental values (gray diamonds) come from the literature [Gardner et al. 1995; Martel et al. 1998; Scaillet and Evans 1999; Pichavant et al. 2002; Grove et al. 2003; Villiger et al. 2006; Andújar et al. 2008; Pietranik et al. 2009; Tomiya et al. 2010; Almeev et al. 2013; Blatter et al. 2013; Rader and Larsen 2013; Waters and Lange 2017]. [C] The mol% An in anorthoclase measured in anorthoclase and plagioclase rims (gray circles), calcic plagioclase compositions measured in the interior of anorthoclase crystals (gray crosses), and sieved plagioclase cores (white) are shown as a function of the An# of the glass. rhyolite-MELTS predicted plagioclase-glass composition pairs are shown for LSR glasses (stippled field) and HSR glasses (gray field). The experimental values (gray diamonds) are taken from the literature [Grove et al. 1982; Juster et al. 1989; Grove et al. 1997; Blatter and Carmichael 2001; Brugger et al. 2003; Couch et al. 2003; Martel and Schmidt 2003; Larsen 2006; Tomiya et al. 2010; Martel 2012; Castro et al. 2013; Waters and Lange 2015; Marxer and Ulmer 2019]. [D] The mol% Or in sanidine measured in sanidine rims (gray circles) are shown as a function of Or# of the glass. rhyolite-MELTS predicted sanidine-glass composition pairs are shown for both LSR and HSR glasses (stippled area). The experimental values (gray diamonds) are taken from the literature [Scaillet 2003; Harms et al. 2004; Gerke et al. 2005; Andújar et al. 2008; Fabbrizio and Carroll 2008; Almeev et al. 2012; Andújar et al. 2013; Martel et al. 2013; Gardner et al. 2014; Bolte et al. 2015; Befus and Gardner 2016; Waters and Andrews 2016; Grocke et al. 2017; Romano et al. 2018; 2020]. All experiments were buffered at QFM, NNO, or Re-ReO₂, consistent with the oxygen fugacity range of the post-collapse rhyolites.

flect the entire ranges of Ti, Al, and Na contents observed in the dataset (Supplementary Material 3 Figure S8 and Supplementary Material 2 Table S8). It is possible that some fraction of the hornblende phenocrysts and microlites are xenocrystic, however, we lack a secondary equilibrium test to exclude them. The partitioning of Ti, Al, and Na into hornblende is known to be partially dependent on temperature, pressure, or melt composition [Sato 2005; Molina et al. 2015; Mutch et al. 2016], such that changes to some intensive variables (i.e. cooling or decompression) could cause a shift in the horn-



blende composition. It is not possible to estimate the hornblende composition in equilibrium with the matrix glass without some $a\ priori$ knowledge of the intensive variables of the Banco Bonito rhyolite. Therefore, we acknowledge the possibility that some of the hornblende in Banco Bonito is not in equilibrium with the matrix glass and/or is xenocrystic, de-

Figure 7: [left] Pre-eruptive storage conditions of the postcollapse rhyolites are compared to the UBT. [A] Temperatures and their $\pm 2\sigma$ uncertainties are shown for each sample based on Fe-Ti oxide (squares), hornblende (diamonds), and clinopyroxene (gray triangles) thermometry. Rhyolites are organized by relative age, from the youngest (on the left) to the oldest (on the right), in all panels. Mineral chemistry from Battleship Rock Ignimbrite (BRI) is collected from Ren and Parker [2019] and used in subsequent subpanels. UBT units are grouped by ovals to differentiate between eruptive units. [B] Sample f02 shown as $\triangle NNO$, calculated with Fe-Ti oxides. [C] The wt% H₂O in equilibrium with anorthoclase and plagioclase rims in each sample are shown and determined based on incorporation of glass compositions and pre-eruptive temperatures from Fe-Ti oxides (squares), hornblende (diamonds), and clinopyroxene (gray triangles) into a plagioclase hygrometer. In [C], T = Fe-Ti Oxides indicates the wt% H2O calculated with Fe-Ti oxide temperatures; T = Hbld indicates the wt% H_2O calculated with hornblende temperatures; T = CPX indicates the wt% H_2O calculated with clinopyroxene temperatures. [D] Storage pressures based on volatile solubility [VESIcal; lacovino et al. 2021] are shown for each sample using temperatures inputs and wt% H₂O based on Fe-Ti oxides (squares), hornblende (diamonds), and clinopyroxene (gray triangles). In [D], T= Fe-Ti Oxides indicates the pressure calculated with Fe-Ti oxide temperatures and wt% H_2O ; T = Hbld indicates the pressure calculated with hornblende temperatures and wt% H_2O ; T = CPX indicates the pressure calculated with clinopyroxene temperatures and wt% H₂O. Pressures derived from hornblende barometry are also shown as gray circles, where average values are black circles, and the $\pm 2\sigma$ in hornblende barometry is calculated based on variation in hornblende compositions. References are as follows: (1) Ren and Parker [2019], (2) Balsley [1988], (3) Warshaw and Smith [1988], (4) Dunbar and Hervig [1992], and (5) Waelkens et al. [2022].

spite general agreement with the $^{\text{Fe-Mg}}\text{K}_D$ values from the literature.

Orthopyroxenes and clinopyroxenes from San Antonio and Banco Bonito have Mg#s between 69.1–74.5 and $^{\rm Fe-Mg}{\rm K}_{\rm D}$ values between 0.11–0.15 and overlap with compositions grown in experiments on rhyolites and dacites which have Mg#s that range from 50–76 (Figure 6B) and $^{\rm Fe-Mg}{\rm K}_{\rm D}$ values of 0.1–0.5. Two orthopyroxenes in San Antonio have Mg#s of 82.2 and 82.3, which have $^{\rm Fe-Mg}{\rm K}_{\rm D}$ values that do not agree with those determined by equilibrium experiments (Figure 6B). We consider the orthopyroxenes in the rhyolite from San Antonio to be xenocrystic to the melt.

The consistent overlap between the compositions of mafic phases grown in experiments and those observed in the post collapse rhyolites (with the exception of orthopyroxene and possibly hornblende in Banco Bonito) (Figure 6A–B; Tables 7, 8 and 9; and Supplementary Material 3 Figure S8) coupled with the homogenous, unzoned, and typically euhedral appearance of the majority of mafic silicates (Figure 5) and lack of reaction textures [e.g. reaction rims; Speer 1987; De Angelis et al. 2015] suggests that the majority of mafic phases in the rhyolites could be phenocrys-

tic. There is two to three times the variation in Ti, Al, and Na contents in hornblende from Banco Bonito than is observed in the other rhyolites (Supplementary Material 3 Figure S8), and, despite this variation, they agree with $^{\text{Fe-Mg}}K_{\text{D}}$ values obtained from experiments. Thus, we cannot exclude any hornblende composition based on our equilibrium test. We used rhyolite-MELTS (v 1.2.0) of Gualda et al. [2012] to estimate mineral compositions for the post-collapse rhyolites as an additional test for hornblende and pyroxene equilibrium; however, no rhyolite-MELTS simulation saturated hornblende and the predicted pyroxene compositions yielded Mg#s that resulted in Fe-MgK_D values that were higher than any currently reported in the experimental literature. Our literature search for buffered equilibrium experiments on high-silica rhyolites that saturated and reported compositions for biotite and hornblende returned six total studies and highlights a notable gap in the experimental literature. The absence of studies that report compositions for hydrous mafic silicates is a limiting factor on our ability to effectively evaluate the petrogenesis of the mafic silicates within the rhyolites. Finally, we could not evaluate mafic silicate equilibrium in Redondo Creek, due to the lack of glass analyses owing to the devitrified glass matrix in the sample.

We evaluate equilibrium in feldspars by comparing feldspar-matrix glass compositions measured in the postcollapse rhyolites (Tables 4 and 5) to feldspar-rhyolite pairs from experiments [e.g. Waters and Lange 2013; Waters and Frey 2018]. Anorthite contents of anorthoclase rims and An# of matrix glasses for rhyolites from Cerro Del Abrigo, Cerro Santa Rosa, Cerro San Luis, Cerro Seco, South Mountain, and San Antonio are outside the available experimental literature (i.e. experimental literature has higher liquid An#s; Figure 6C), however, the pairs fall along the trend of low An ($\langle An_{15} \rangle$) anorthoclase in melts with low An# (≤ 5) predicted by the experimental dataset (Figure 6C). Additionally, we input the matrix glass analyses for HSRs and LSRs into rhyolite-MELTS (v 1.2.0) [Gualda et al. 2012] and equilibrated those melt compositions over a range of temperatures (800– 700 °C) and pressures (100-300 MPa) under fluid-saturated conditions to determine the range of feldspar compositions predicted for very evolved rhyolites (shown as fields in Figure 6C–D). We find that rhyolite-MELTS predicts anorthoclase and plagioclase compositions for HSRs that overlap with our measured anorthoclase rim compositions for the HSR rhyolites, and the LSR San Antonio (Figure 6C). Moreover, the euhedral textures associated with rims of anorthoclase (Figure 2) from Cerro Del Abrigo, Cerro Santa Rosa, Cerro San Luis, Cerro Seco, South Mountain, and San Antonio further suggests that the anorthoclase rims and matrix glasses are in equilibrium.

The trace An-rich cores in anorthoclase (Figure 3B, C, E, and F) in rhyolites from Cerro Del Abrigo, Cerro Santa Rosa, Cerro Seco, San Antonio, and some sieve texture plagioclase in the rhyolite from Banco Bonito (Figure 2D and Figure 3H) are more calcic (>30 mol% An) than any experimentally grown anorthoclase composition in a melt with low An# (<5; (Figure 6C) and are xenocrystic or antecrystic. We find that the sieve-textured plagioclase cores in Banco Bonito are similar to

those produced by dissolution due to heating [e.g. Tsuchiyama and Takahashi 1983; Landi et al. 2004; Acosta-Vigil et al. 2006]. However, the rims on plagioclase with sieve-textured cores in Banco Bonito are homogeneous with well-defined edges (i.e. lacking resorption textures; Figure 2D and Supplementary Material 3 Figure S5) and overlap with experimental plagioclase compositions (Figure 6C). Thus, the rims are likely in equilibrium with the matrix glass, though plagioclase in Banco Bonito still has a higher mol% An than that predicted by rhyolite-MELTS for LSR compositions (Figure 6C). We note that some of the sieve textures in Banco Bonito have compositions that extend to lower An-contents (20-25 mol% An; Figure 3H), and overlap with the rim compositions (Figure 6C) and with the experimental dataset. The compositions of the sieve textures that overlap with rims and the experimental dataset are always associated with areas of plagioclase located adjacent to melt inclusions. To maintain a consistent dataset, we only use plagioclase compositions measured on crystal rims (Table 4) in Banco Bonito to evaluate equilibrium with the matrix glass.

We also compare sanidine and glass pairs with those equilibrated in experiments and find agreement between compositions measured in the natural samples and experimental values. Given the euhedral sanidine textures (Figure 4), nearly homogeneous compositions in a single sample (Figure 3), and overlap with experimental data (Figure 6D), it is likely that all sanidines in the post-collapse rhyolites are phenocrystic. The sanidine compositions predicted by rhyolite-MELTS [Gualda et al. 2012] overlap well with sanidine in Cerro Del Abrigo, San Antonio, and South Mountain (Figure 6D). Sanidine in Cerro Santa Rosa, Cerro San Luis, and Cerro Seco are just outside the predicted compositions (Figure 6D) but still within experimental values, so we consider them to be phenocrystic. While no sanidine was found in our entire thin section of the Banco Bonito flow outside of the crystalline clots (Supplementary Material 3 Figure S2), Zimmerer et al. [2016] successfully calculated ⁴⁰Ar/³⁹Ar ages from sanidine found in their samples, and Eichler and Spell [2020] find a total modal abundance of ~4% sanidine in samples of Banco Bonito obsidian, suggesting that the flow is heterogeneous. Alternatively, it is possible that the sanidines in Banco Bonito are inherited crystals, as LSRs with compositions similar to Banco Bonito do not typically saturate sanidine until near-solidus conditions [e.g. MLV-36 from Waters et al. 2015]. For comparison, the Fe-Ti oxides in our sample of Banco Bonito returned a temperature of 790 °C (Table 6), whereas our rhyolite-MELTs equilibration simulations that utilized the Banco Bonito matrix glass only saturated sanidine at temperatures ≤740 °C.

5.3 Summary of mineral-melt equilibrium

In summary, we find that the compositions of anorthoclase/plagioclase and sanidine rims and matrix glasses in the post-collapse rhyolites (Figure 6C and D) are likely in equilibrium (i.e. phenocrystic) on the basis of composition and texture. The majority of the mafic silicates also appear to be in equilibrium with the matrix glass given the average $^{\rm Fe-Mg}{\rm K}_{\rm D}$ values associated with mafic silicates along with their euhedral, unzoned textures (Figure 6A and B). We note there is

variation in hornblende composition (on the basis of Na, Ti, and Al contents) in Banco Bonito, such that some hornblende may be xenocrystic, but we cannot exclude them based on our current equilibrium test. We identify xenocrystic orthopyroxene in the rhyolite from San Antonio though we cannot determine the origin of these orthopyroxenes as there is no other evidence of mixing in the sample (i.e. the sample has homogeneous glass analyses and groundmass texture in thin section and hand sample; Table 3 and Supplementary Material 3 Figure S1H). The abundant sieved cores in anorthoclase in Banco Bonito (3.5% of the sample) and the trace (<1% of the sample) anorthite-rich plagioclase cores in anorthoclase crystals (24– 48 mol% An; Figure 3B, C, E, and F) from Cerro Del Abrigo, Cerro Santa Rosa, Cerro Seco, and San Antonio (Supplementary Material 3 Figure S3–S5) are also likely xenocrystic or antecrystic (Figure 6C).

We also note that there are very few experiments available in the literature for comparison for evolved HSRs with compositions similar to our matrix glasses, which limited our ability to evaluate the origins of minerals within the rhyolites in this study. While rhyolite-MELTS is a useful tool for predicting the feldspar-liquid equilibrium, it is calibrated on existing experimental datasets. Given both the lack of experiments on low-MgO, high-SiO₂ liquids and a lack of activity models for many multicomponent hydrous phases (i.e. hornblende, biotite), it is not surprising that rhyolite-MELTS did not successfully saturate biotite or hornblende in fluid-saturated equilibration runs for our matrix glass compositions. Therefore, while using rhyolite-MELTS as a predictive tool appears to be robust for extrapolating feldspar-liquid equilibrium, its utility for predicting equilibrium between liquids and mafic silicates is limited for these compositions, owing to the lack of experimental data and activity models for mafic, hydrous minerals.

5.4 Calculation of intensive variables recorded by silicate minerals and glasses

We apply model thermometers to hornblende and clinopyroxene compositions in the rhyolites to augment the temperature estimates from the Fe-Ti oxides. Temperatures from hornblende and clinopyroxene thermometry from the rhyolite from Banco Bonito should be viewed with caution, given that a subset of these crustals may be xenocrustic. We applied the pressure-independent hornblende thermometer of Putirka [2016] (eq. 5 from their study, which has a standard error estimate (SEE) of ± 30 °C) to crystals from our samples. Hornblende compositions from the post-collapse rhyolites yield temperatures ($\pm 2\sigma$) ranging from 733 \pm 20 °C (Seco) to 835 ± 67 °C (Banco Bonito), where the standard deviation reflects the range of hornblende compositions within individual rhyolites (Figure 7A). For all hornblendes, the range of temperatures due to analytic error is $\leq 17\,^{\circ}$ C, which is less than the range of temperatures from all hornblende compositions and less than the associated model error (Figure 7A and Table 8). Additionally, we applied the clinopyroxene-liquid thermometer of Putirka [2008] (eq. 33 from their study, SEE = ± 42 °C) to clinopyroxenes and glass compositions from San Antonio and Banco Bonito, which record temperatures of 823 ± 10 °C and 799 ± 5 °C (Table 9), respectively, where the standard deviation reflects the range of clinopyroxene compositions in a sample.

We applied the plagioclase-hygrometer of Waters and Lange [2015] to our anorthoclase and plagioclase rim-glass pairs at the average temperatures recorded by Fe-Ti oxides, hornblende, and clinopyroxene to estimate pre-eruptive H₂O contents (Table 4 and Figure 7C), where the error associated with the H₂O contents reflect the $\pm 2\sigma$ values associated with each pre-eruptive temperature. The average pre-eruptive H_2O contents range from 4.4–6.0 wt% H_2O , as recorded by average temperatures (Figure 7A), anorthoclase and plagioclase rims, and interstitial glasses, with a model SEE = 0.35 wt% H₂O (Figure 7C). Average H₂O contents vary by as little as 0.1 wt% in a single sample (e.g. Cerro Del Abrigo; Table 4 and Figure 7C), when the applied thermometers are in agreement, but can vary by as much as 2.0 wt% when the thermometers record more disparate temperatures (e.g. San Antonio; Table 4 and Figure 7C). The HSR rhyolites, Cerro Santa Rosa, Cerro San Luis, and Cerro Seco, have anorthoclase with the most sodic rims (An₈; Table 4) and the coldest pre-eruptive temperatures (742-754°C; Table 6 and Figure 7A), which yield the highest average H₂O contents. The LSR rhyolites, San Antonio and Banco Bonito, with average temperatures of 788-809 °C and the most calcic rims (An₁₃₋₂₂; Table 4) have the lowest average H₂O contents (Figure 7C).

We apply the temperature-independent hornblende barometer of Mutch et al. [2016], which calculates pressures (SEE = ±50 MPa) based on total Al-in-hornblende in silicic melt, to hornblendes in our samples. We find that hornblende in all rhyolites except for Banco Bonito records average pressures ranging from 154 ± 70 MPa to 203 ± 22 MPa, corresponding to \sim 6-8 km based on a crustal density of 2700 kg m⁻³ (Table 8), where the reported standard deviation reflects the range of hornblende compositions measured in each sample. Hornblendes in Banco Bonito record a wider range of pressure from 157-376 MPa (~6-14 km), which is based on the range of hornblende compositions in that sample. Hornblende rims and microlites record the entire range of pressures in the sample (i.e. rims and microlites do not record common pressures; Figure 7D and Supplementary Material 3 Figure S8), and we cannot ascribe one pressure range to Banco Bonito within our data. Hornblende crustals in Banco Bonito appear homogenous in BSE images (Figure 5 and Supplementary Material 3 Figure S8) and there is no consistent pattern in pressure between core or rim analyses. For example, in two different hornblende crystals the core compositions, which are relatively depleted in Ti, Al, and Na, record pressures from 157–199 MPa and the rims, which are enriched in Ti, Al and Na, record higher pressures ranging from 223–308 MPa (Supplementary Material 3 Figure S8). Other hornblendes have homogeneous compositions where there is little to no variation in pressures recorded by cores and rims. Hornblende microlites (≤50 µm) that are located within microns of each other in a thin section (and appear to have the same composition in BSE) contain enough variation in their Ti, Al, and Na contents to yield a range of pressure from 174 to 337 MPa (where the hornblende microlites enriched in Ti, Al, and Na record higher pressures). Thus, Banco Bonito appears to be heterogeneous on a micron scale and we cannot determine which segment of the total pressure range reflects the pre-eruptive storage conditions (Figure 7D).

As a secondary estimate of pre-eruptive storage pressures, we utilize the thermodynamic model VESIcal of lacovino et al. [2021] for mixed volatile solubility in silicate melts. We apply the MagmaSat model [Ghiorso and Gualda 2015] for pure-H₂O solubility to H₂O contents obtained from plagioclasehygrometry to estimate pre-eruptive pressures. The average pressures that correspond to the H₂O contents associated with the post-collapse rhyolites (Table 4) span a range from 82-194 MPa (\sim 3–7 km based on a crustal density of 2700 kg m⁻³) using all calculated temperatures (Table 4). These pressures correspond to the conditions at which the anorthoclase and/or plagioclase rims were growing in each melt, as they are calculated based on H₂O contents obtained from plagioclasehygrometry. We calculate a minimum uncertainty $(\pm 2\sigma)$ of ±40 MPa for all pure-H₂O saturation pressures, based on the SEE of the plagioclase hygrometer (± 0.35 wt% H_2O). We show $\pm 2\sigma$ in pressure in Figure 7D where the lowest pressure is calculated using inputs of the hottest possible temperatures and lowest H₂O and the highest possible pressure is calculated using the lowest possible temperature and the highest water contents. Rhyolites that have mineral assemblages that appear to record little variation in pressure also have temperatures from Fe-Ti oxides and other mafic phases that span a narrow range (e.g. Cerro Santa Rosa; Table 6 and Figure 7D).

5.5 Summary of intensive variables

For the HSRs (Cerro Del Abrigo, Cerro Santa Rosa, Cerro San Luis, Cerro Seco, and South Mountain), the average temperature recorded by hornblende (Figure 7A and Table 8) and the average temperatures recorded by Fe-Ti oxides (Table 6 and Figure 7A) vary by ≤ 35 °C, where the total range in average temperatures is from 733–771 °C. The LSRs (Redondo Creek, San Antonio, and Banco Bonito) have mineral assemblages that record temperatures that differ by more than 50 °C. Temperatures recorded by hornblende are systematically colder than those recorded by Fe-Ti oxides (with the exception of South Mountain) which is overall consistent with phase equilibrium experiments on rhyolites where hydrous phases typically saturate at lower temperatures than Fe-Ti oxides [e.g. Bishop Tuff and Glass mountain; Gardner et al. 2014; Waters and Andrews 2016, respectively]; however, this shift is not resolvable within model errors for our results, so we note it as of interest but draw no further conclusions. We apply the same thermometers, hygrometers, and barometers to the Battleship Rock Ignimbrite (BRI) using mineral and glass data from Ren and Parker [2019] to expand the number of East Fork rhyolites. Despite the variety of processes that are recorded by multiple thermometers (i.e. the timing of mineral saturation), the HSRs share a common range of average pre-eruptive temperatures from ~733 °C to ~771 °C (Figure 7A), and LSRs Banco Bonito, Battleship Rock, and Redondo Creek are systematically hotter, with pre-eruptive temperatures ranging from ~790 to 835 °C. We note that the temperatures from San Antonio (an LSR) fall along this trend but are not resolvable within the standard error of the applied models (Figure 7A).

Oxygen fugacities in all the post-collapse rhyolites, calculated using the Fe-Ti oxide barometer of Ghiorso and Evans [2008] range from of -0.1 to +1.3 ΔNNO (Table 6 and Figure 7B). Redondo Creek is slightly above the NNO buffer at +0.4 ΔNNO . The Valle Grande rhyolites are typically more reduced, with a range in fO_2 s from -0.1 to +0.4 ΔNNO (Table 6). Banco Bonito is the most oxidized post-collapse rhyolite at +1.3 ΔNNO (Table 6). Similarly, Battleship Rock is also oxidized with Fe-Ti oxides recording an oxygen fugacity of +1.2 ΔNNO (Figure 7B).

When pure-H₂O solubility pressures match hornblende barometry pressures it is likely that anorthoclase and/or plagioclase and hornblende equilibrated at similar depths. For the HSRs, the pressures that correspond to water contents recorded by anorthoclase and plagioclase, and those obtained from hornblende barometry are similar (Figure 7D). There is less agreement between different estimates of pre-eruptive pressures for the LSRs (Figure 7D). Pre-eruptive pressures for San Antonio are consistent with the HSRs, using temperatures from Fe-Ti oxides and hornblende (Figure 7D) and are shallower than the HSRs when using elevated clinopyroxene temperatures (Figure 7D and Table 9). For the youngest LSRs, Banco Bonito and Battleship Rock, the average pressure estimates from hygrometry and the MagmaSat solubility model in VESIcal are consistent with the storage depths of the HSRs (Figure 7D). However, hornblende barometry [i.e. the model of Mutch et al. 2016 typically records higher pressures than those estimated using the solubility model.

There are three explanations that could account for the discrepancy between hornblende-derived pressures and those estimated using the solubility model. (1) There are xenocrystic hornblende in the young LSRs that we could not identify using our methods and/or the unit is thoroughly mixed so that it is heterogeneous on a micron scale. (2) Crystallization of hornblende occurred during decompression and/or cooling. In such a scenario, none of the hornblende are xenocrystic and could be grown during a dynamic process (i.e. decompression or cooling), which would account for the euhedral textures observed in nearly all hornblende phenocrysts and microlites. However, we still cannot determine phenocryst from xenocrust in this scenario. (3) Finally, an important difference between the two estimates of pressures is that the hornblende barometer of Mutch et al. [2016] estimates P_{Total} , and the pressure estimates from the solubility model reflect the partial pressure of H₂O. It could be the case that pressure estimates from a solubility model and H₂O contents agree with the hornblende barometer when $P_{\text{H}_2\text{O}}$ approximates P_{Total} , and the fluid phase in the magma consists mostly of H₂O. However, in systems that may contain an additional volatile phase (e.g. abundant CO₂), comparable water contents require higher pressures, thus mineral barometers recording P_{Total} have the potential to record higher pressures than any estimates of $P_{\text{H}_2\text{O}}$. A detailed melt inclusion study of the LSRs from the East Fork Member would provide volatile contents that could be used to more rigorously constrain the preeruptive pressures of the young eruptions from Valles Caldera and clarify the apparent discrepancy in this current dataset.

Given our dataset and recent work by Wolff and Neukampf [2022] that found heterogeneity in glasses within the Battleship Rock Ignimbrite, we suggest that hypothesis (1), where hornblende crystals are either xenocrysts or grown in melts that are mixed on a micron scale, is the most likely. If the microlites are indeed growing from unique melts mixed on a fine scale, it is worth pointing out that their pressures may indicate the different source depths of these melts (Supplementary Material 3 Figure S2), as the hornblende barometer of Mutch et al. [2016] only utilizes hornblende compositions as inputs. Therefore, as of now, we cannot provide a refined estimate for the pre-eruptive storage pressure of the youngest eruptions from Valles Caldera, owing to the uncertainties about the origin of hornblende in the rhyolite from Banco Bonito. Though we observe heterogeneity in the hornblendes, we note that Fe-Ti oxides can reset and reach equilibrium within a week [Hou et al. 2021]. Moreover, the magnetite-ilmenite pairs we utilized in Banco Bonito passed the equilibrium test of Bacon and Hirschmann [1988] and yield a narrow range of temperature and oxygen fugacity, which suggests they record an accurate range of pre-eruptive temperatures and oxygen fugacities.

Overall, the pre-eruptive storage conditions of HSRs that erupted immediately following the UBT are 733 to 772°C, -0.1 to +0.4 Δ NNO, 4.8 to 6.0 wt% H₂O, and 149 to 196 MPa. The Valle Grande rhyolites are remarkably consistent in their overall mineralogy (Supplementary Material 3 Figure S1), including modal abundance of phenocrysts (Table 1) and the compositions of the feldspars (Figure 3), present in the rhyolites up until the eruption of the LSR San Antonio. The euhedral mineral textures and equilibrium tests that showed that the majority of the mineral rims grew from the melt suggest that the mineral assemblage equilibrated at relatively static conditions prior to eruption, where no significant mixing event or heating event occurred (or was recorded in the mineral assemblage). If the minerals had crystallized under rapid heating or mixing events, we would not expect the minerals to be in chemical or textural equilibrium with the glass. The youngest LSR eruptions from Valles Caldera typically have pre-eruptive storage conditions of >800 °C, +1.2 to $+1.3 \Delta NNO$, 3.8 to 6.1 wt% H_2O , and 86 to 376 MPa. Our results suggest that Banco Bonito likely formed during a heating event of a magma body, which generated the sieve textured plagioclase cores. The thick rims on the plagioclase cores in Banco Bonito (~20 μm; Supplementary Material 3 Figure S5) could have grown either following the heating event at depth in the presence of a mixed volatile phase (i.e. low P_{H_2O}) or at shallow pressures (Figure 7D); we can make no distinction using our dataset. We find that the East Fork Member marks a significant change in mineralogy, where mafic minerals are in greater abundance, and there are significant xenocrysts and xenocrystic crystalline clots, which is consistent with many previous works [Self et al. 1988; Spell et al. 1993; Wolff and Gardner 1995; Goff et al. 2011; Wolff et al. 2011; Zimmerer et al. 2016; Eichler and Spell 2020; Nasholds and Zimmerer 2022; Wolff and Neukampf 2022].

The main difference between the post-collapse rhyolites is that the youngest LSRs have higher average pre-eruptive temperatures and are more oxidized than the Valle Grande Mem-

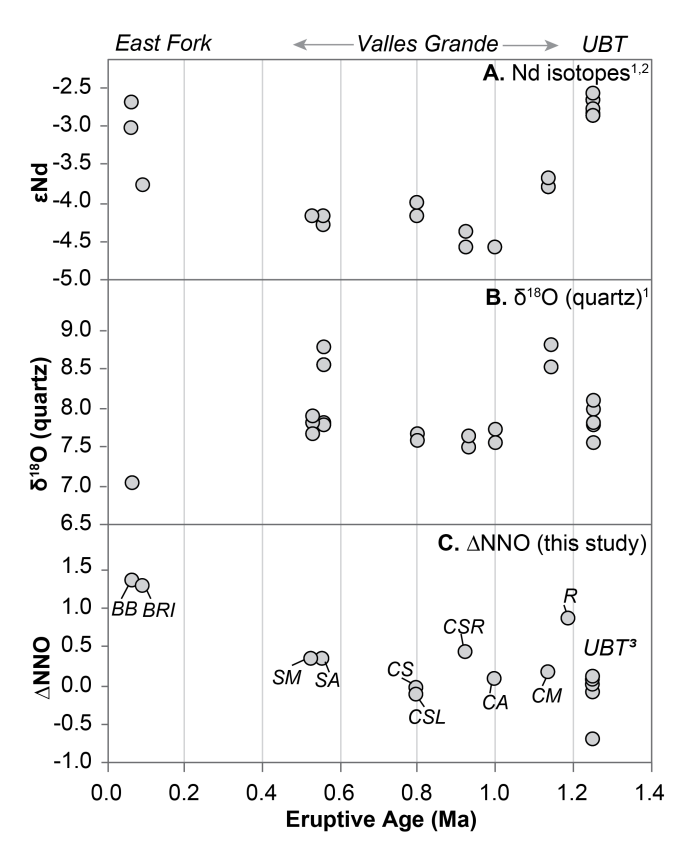


Figure 8: Isotope data from the literature and sample fO_2 (as a function of Δ NNO) for the UBT and post-collapse rhyolites from this study are shown as a function of their eruptive ages. [A] The ϵ_{Nd} values in the post-collapse rhyolites [Spell et al. 1993; Eichler and Spell 2020] and UBT [Skuba 1990] are compared to eruptive age. [B] The δ^{18} O values in quartz in the post-collapse rhyolites [Spell et al. 1993] and UBT [Skuba 1990] are compared to eruptive age. [C] Δ NNO shown relative to eruptive ages, showing the same oxidation data as in Figure 7B. Superscript references are as follows: (1) Spell et al. [1993], (2) Skuba [1990], and (3) Warshaw and Smith [1988]. See text for discussion of this figure.

ber. The youngest eruptions also contain a greater xenocrystic load than the Valle Grande rhyolites, seen both through petrology, and geochronology [Self et al. 1988; Zimmerer et al. 2016; Nasholds and Zimmerer 2022; Wolff and Neukampf 2022], which suggests the petrologic processes that led to the formation of the East Fork Member are distinct from the previously erupted Valle Grande Member. Despite considerable heterogeneity in the youngest eruptions from Valles Caldera, there is homogeneity in the intensive variables of the Valle Grande HSRs, suggesting the Valle Grande rhyolites were all stored under similar conditions (Figures 7 and 8).

5.6 Evolution of a post-collapse magmatic system

We compare the intensive variables recorded by the post-collapse rhyolites to the UBT to understand how and when the conditions of the magmatic system changed following the caldera-forming eruption. Temperatures and ΔNNO values determined from fayalite, spinel, and Fe-Ti oxides vary

across units within the UBT, where unit 1 average temperatures range from 700–726 °C with an average oxygen fugacity of ΔNNO -0.7, and units 2-4 show a range in temperature from 750–810 °C and an average ΔNNO of -0.7 (Figure 7A and B). There is a shift in temperature and oxygen fugacity in unit 5 where it has on average higher temperatures from 770-837 °C (Figure 7A and B) and is more oxidized with average Δ NNO from -0.1 to +0.1 [Balsley 1988; Warshaw and Smith 1988; Wilcock et al. 2013]. We utilize the unit names provided by Warshaw and Smith [1988]. A detailed summary of the different naming schemes, and unit correlation between studies, for different sub-units of the UBT is provided in Goff et al. [2014] and Wilcock et al. [2013]. Volatile contents measured in melt inclusions from the plinian air fall of the UBT (Tsankawi pumice) range from 2.8–5.0 wt% H₂O (Figure 7C) and 34–147 ppm CO₂, which correspond to entrapment pressures (i.e. total pressures) of 100-143 MPa, or ~4-5 km [Figure 7D; Dunbar and Hervig 1992; Waelkens et al. 2022]. Our results suggest that the post-collapse rhyolites are generated at similar conditions to the UBT [Warshaw and Smith 1988; Dunbar and Hervig 1992; Waelkens et al. 2022] with the exception that the system has become more oxidizing since the eruption of the UBT, and more recent eruptions are sourced from greater pressures (Table 6 and Figure 7A–D).

Redondo Creek erupted immediately following the eruption of the UBT and has a similar pre-eruptive temperature of 824°C to unit 5 of the UBT but records conditions that are more oxidizing (Δ NNO +0.4; Table 6 and Figure 7B) than the UBT. Following the eruption of Redondo Creek, Cerro Del Medio erupted as the first intra-caldera dome in the southeast quadrant (Figure 1) with an intermediate temperature at 772 °C (Figure 7A) and an fO_2 of $\Delta NNO +0.2$ (Table 6 and Figure 7B). No further details about the pre-eruptive conditions of these rhyolites could be assessed owing to lack of glass in the sample from Redondo Creek and lack of phenocrysts in the Cerro Del Medio obsidian. Following the eruption of Cerro Del Medio, the HSR rhyolite domes Cerro Del Abrigo, Cerro Santa Rosa, Cerro San Luis, and Cerro Seco erupted from 1010-800.3 ka (Figure 1), with average temperatures ranging from 750-771 °C (from Fe-Ti oxide thermometry) and 733–757 °C (from hornblende thermometry), which are indistinguishable from each other when considering errors associated with each model thermometer (Figure 7A). Mean fO₂ For Cerro Del Abrigo, Cerro San Luis, and Cerro Seco ranges from -0.1 to +0.1 Δ NNO, while Cerro Santa Rosa is slightly more oxidized at +0.4 Δ NNO. Mean H₂O contents for these rhyolites range from 5.1-6.0 wt% H₂O (Figure 7C), and pressure estimates for both $P_{\text{H}_2\text{O}}$ and P_{Total} are within model agreement, suggesting common storage pressures between 145–196 MPa, or \sim 5–7 km depth (Figure 7D) indicating relatively shallow storage in the upper crust.

The era of post-collapse volcanism dominated by HSRs at Valles Caldera was followed by predominantly LSR eruptions from 563–68.9 ka [Nasholds and Zimmerer 2022]. The average temperature of San Antonio (784 °C; Figure 7A) is slightly hotter than the previous HSRs, though temperatures are not resolvable given the standard errors associated with individual thermometers (Figure 7A). San Antonio is slightly more

oxidized than the previous eruption (Cerro Seco with -0.1 ΔNNO) at +0.3 ΔNNO (Figure 7B). The average H_2O contents for San Antonio are also lower than the preceding eruption at 4.6 wt% H₂O (Figure 7C) and spans a wider range due to disparate temperatures (Table 4). However, P_{Total} and average $P_{\rm H_2O}$ for San Antonio are within model error at 154 MPa and 124 MPa, respectively (Figure 7D). The next eruption, South Mountain (534.8 ka), marks a shift back to a HSR, as well as a geographic shift to the opposite side of the caldera floor in the south-east quadrant (Figure 1). South Mountain is similar to the other HSRs with a colder pre-eruptive temperature of 753 °C and mean H₂O contents of 5.2 wt% H₂O (Figure 7A) and C). However, with a $+0.4 \Delta NNO$, South Mountain follows San Antonio in being slightly more oxidized (Figure 7B). Total pressure (203 MPa) and $P_{\mathrm{H}_{2}\mathrm{O}}$ (153 MPa), agree within model error, and indicate a range of storage pressures similar to the older HSRs with depths of \sim 6–8 km (Figure 7D).

Since the eruption of the UBT, the overarching trend is that the Valles system has become increasingly oxidized, shifting from an oxygen fugacity at the QFM buffer ($-0.7 \Delta NNO$) with the eruption of units 1–4 of the UBT, to $\sim+0.4$ ΔNNO at the onset of initial post-collapse volcanism, and increasing to $\sim +1$ Δ NNO with two of the East Fork rhyolites (Figure 7B). The elevated oxugen fugacities recorded by Fe-Ti oxides in the post-collapse eruptions are consistent with the observed phase assemblages (Table 1) in the rhyolites [e.g. biotite and hornblende; Carmichael and Ghiorso 1990]. The onset of this change in oxygen fugacity occurred 32 ka [Nasholds and Zimmerer 2022 after the eruption of the UBT, with the eruption of Redondo Peak, and continued through the East Fork eruptions (Figure 7B). A perplexing aspect to these results is that, despite a significant change in oxygen fugacity (Figure 7B), the preeruptive storage pressures for the UBT and the Valles Grande Member of the post-collapse rhyolites are indistinguishable (Figure 7D), which raises the question: are the Valles Grande rhyolites (and possibly the younger East Fork Rhyolites) genetically related to the magmatic system that sourced the UBT?

The Valles Caldera region has a long history of erupting oxidized rhyolites. The Valle Toledo Member, which preceded the eruption of the UBT, is mostly comprised of variably oxidized, small (<20 km³) eruptions [Heiken et al. 1986; Gardner et al. 2010; Goff et al. 2011; Kelley et al. 2013; Meszaros et al. 2023, with few (n = 5) eruptions of faulite-bearing tephra [Meszaros et al. 2023]. Therefore, we evaluate the magmatic system with the assumption that the post-collapse rhyolites represent the background, oxidized magmatic system that generally underlies the Valles Caldera region. We find that there are two possible hypotheses for how magmas that erupted in close spatial and temporal proximity to each other can have dramatically different oxidation states at a common pre-eruptive pressure. (1) Evidence from isotopic analyses [Spell et al. 1993; Eichler and Spell 2020] and geochronology [Wu et al. 2021] suggest that the oxidized magmatic system at Valles Caldera is periodically infiltrated by rapidly accumulated, reduced, fayalite-bearing melt (i.e. the UBT). In such a scenario, the reduced melt may originate from a different source in the crust, share a common pre-eruptive storage depth with the post-collapse rhyolites (Figure 7D), and reach its cumulative volume over a relatively short time span. Following the evacuation of the reduced rhyolite, oxidized volcanism resumes (i.e. the Valles Grande rhyolites). (2) Alternatively, the source of the oxidized rhyolites is also the magmatic source of the UBT, in which case a significant change to the mineralogy and fO_2 of the entire magmatic system is required. A recent experimental and petrological study on the Valle Toledo Member (which pre-dates the UBT) by Meszaros et al. [2023] suggests that such a change could be generated by an influx of reduced, Cl-rich fluids. Their hypothesis builds on earlier work by Boro et al. [2020], who suggested that the chemistry and petrology of enclaves in the UBT record an influx of fluid generated from the melt of a biotite-rich crystal mush, and by Waelkens et al. [2022], who found the first postcollapse rhyolite, Deer Canyon, was significantly depleted in Cl (1310-2050 ppm) compared to the rest of the UBT (2560-4080 ppm). Meszaros et al. [2023] suggest that a mass of reduced, Cl-rich fluid, equivalent to 0.02% of the mass of the UBT, could reduce a mass of Fe₂O₃ in the oxidized system to form 0.7 wt% FeO, which is enough to shift the system fO2 to that of the QFM buffer and results in the stabilization of fayalite. Meszaros et al. [2023] find that this model best explains resorption textures in biotite and the REE, FeO^T , and Cl contents measured in quartz-hosted melt inclusions in reduced, fayalite-bearing magmas from the Toledo Member. If the reduced fluids ceased to infiltrate the upper crust following the eruption of the UBT, then the magmatic system may have returned to oxidizing conditions (i.e. the Valles Grande Member).

While the hypothesis of Meszaros et al. [2023] may account for petrologic changes and chemical trends in melt inclusions, we find that our work and isotopic evidence in the literature suggests that the source of the post-collapse rhyolites and the source of the UBT are fundamentally different [Skuba 1990; Spell et al. 1993; Eichler and Spell 2020]. We can partially evaluate the possible role of halogen-rich fluids in shifting oxygen fugacity in the Valle Grande rhyolites using halogen contents from our glasses (Table 3). Experimental works [Candela 1986; Bell and Simon 2011] show that open system degassing of halogens preferentially removes ferrous iron from the melt, suggesting that degassing of halogens has the potential to increase magmatic oxidation state and reduce the total iron content of the melt. The samples with the lowest halogen contents (e.g. Banco Bonito; Table 3) have highest oxidation states (Table 6) and also have the highest total iron contents (Table 2). Because the samples with the lowest halogen contents also have the highest iron contents, it is unlikely that the patterns in oxidation state are due to removal of ferrous iron by halogen rich fluids and are ultimately not due to a process like passive degassing. Second, the possibility that the Valle Grande rhyolites mixed with a Cl-rich dacite magma, as seen in the UBT by Boro et al. [2020], is not born out in the petrology of our samples. The rhyolites that contain the highest halogen contents (Cerro San Luis and Cerro Seco) also have the lowest abundance of mafic phases (Table 1), lack enclaves of more mafic (i.e. dacitic) magma, contain homogenous feldspars (Figure 3), and hornblendes that span a narrow range in composition (Figure 7D and Table 8), suggesting the increased halogen contents are not due to interaction with a Cl-rich dacite.

Isotopes from previous works also suggest that the Valle Grande Member was sourced from a magmatic system distinct from the UBT. Previous Nd-isotope analyses from Spell et al. [1993] show that the early post-collapse rhyolites (the Valles Grande HSRs and LSRs) have consistent ϵ_{Nd} values that range from -4.0 to -4.6 and fall between ε_{Nd} values for the UBT [-2.6 to -2.9; Skuba 1990] and the local granitoid basement [-16.4 to -12.8; Skuba 1990] (where ε_{Nd} is defined as $10,000(^{143}Nd)^{144}Nd_{sample}$ – ¹⁴³Nd/¹⁴⁴Nd_{chondrite})/¹⁴³Nd/¹⁴⁴Nd_{chondrite}; Figure 8A). The Nd-isotopes of the Valles Grande are distinct from those of the UBT, differing as much as $\varepsilon_{Nd} = 2$ [Figure 8A; Spell et al. 1993]. The ε_{Nd} values of the East Fork span a continuum between those of the Valles Grande and the UBT, ranging from -2.7 to -3.8 [Figure 8A; Spell et al. 1993; Eichler and Spell 2020]. Chemical and redox variation between the UBT and the Valles Grande Member should be accounted for if the reduced fluids ceased to intrude into the upper crustal magmatic system based on the hypothesis of Meszaros et al. [2023]. However, the cessation of fluid infiltration, which is required to explain the elevated oxidation state of the Valles Grande Member, does not account for the abrupt shift in Nd isotopes between the eruption of the UBT and Valles Grande Member (Figure 8A).

Based on the Nd isotopes (Figure 8A), it would appear that the magmatic system becomes more similar to the UBT in the recent eruptions of the East Fork Member. However, limited oxygen isotope analyses on quartz crystals in the East Fork Member from Spell et al. [1993] reveal the lowest δ^{18} O values out of all samples erupted since and including the UBT (Figure 8B). The low δ^{18} O values suggests that the East Fork Member could have incorporated hydrothermally altered material [Bindeman and Valley 2000; Bindeman et al. 2007; Troch et al. 2020], which may also explain the relatively high oxygen fugacity recorded by their Fe-Ti oxides. In contrast, quartz in the UBT has elevated δ^{18} O values [Skuba 1990], suggesting it incorporated minimal hydrothermally altered material Bindeman and Valley 2000; Bindeman et al. 2007; Troch et al. 2020], and that its source is fundamentally different than that of the East Fork rhyolites. We do note that oxygen isotope data for the East Fork is sparse, and recent work by Wolff and Neukampf [2022] show that $\delta^{18}O$ values of glasses and biotites in Battleship Rock indicate that the unit underwent hydrothermal alteration by meteoric fluids. Thus, without more analyses for the $\delta^{18}O$ values reported for quartz the interpretation of the oxygen isotopes should be treated with caution.

Finally, Wu et al. [2021] find that zircon U-Pb ages measured in the UBT are unimodal, consistent with the eruptive age of the UBT, and reflect no inheritance of zircons with significantly older ages. Wu et al. [2021] attribute the lack of inherited zircons to rapid assembly of the UBT rhyolite in the upper crust, which suggests that it did not form from previous batches of magma (i.e. those which sourced the preceding rhyolite of the Valle Toledo Member). While reducing fluids may alter the mineralogy of a magmatic source, it is not clear how fluids may overprint ages of existing zircon, so as to make one homogeneous age population.

We find that the differences in oxidation states (Table 6, Figure 7B, and Figure 8C) and chemistry (e.g. Figure 8) between the UBT and post-collapse rhyolites, despite a common storage depth (Figure 7D), are best explained if the post-collapse rhyolites and the UBT issue from different sources and are stored at a common location in the crust, given the combined dataset of halogen + total iron contents in glasses (Table 2), neodymium and oxygen isotopes (Figure 8), and zircon ages from the literature. We note that we do not observe petrologic evidence of the post-collapse rhyolites forming from a magmatic system initially saturated in fayalite, such as the UBT. We do not observe resorbed fayalite, fayalite included in biotite, or fayalite heavily mantled with magnetite [Mackwell 1992. We suggest that the transition in oxidation state observed between the UBT and the post-collapse rhyolites (Figure 8C), given a common pre-eruptive storage depth, can be explained if the UBT is ephemeral [Wolff and Ramos 2003] and has a unique, reduced source in the crust [Spell et al. 1993; Wu et al. 2021, along with a unique fluid profile [e.g. Cl-rich and reducing; Boro et al. 2020; Waelkens et al. 2022; Meszaros et al. 2023]. Therefore, the evolution of the magmatic system beneath Valles Caldera appears to involve two sources, where one source generates voluminous, caldera-forming, reduced, fayalite-bearing rhyolites (e.g. UBT and LBT) and another source generates smaller-volume, oxidized rhyolites (e.g. Valles Grande and East Fork Members).

Through conducting this work, we identify several opportunities for further investigation that would provide more insight into the magmatic processes that produced the post-collapse rhyolites. (1) We find that trace element analyses of matrix glasses from the post-collapse rhyolites would provide more insight into the role of magma mixing in the East Fork Member and if any mixing was involved in the formation of the Valles Grande rhyolites. The hornblende microlites with variable compositions provide evidence that the rhyolite from Banco Bonito is heterogenous on a micron length scale and Wolff and Neukampf [2022] observed similar fine scale heterogeneity in matrix glasses in Battleship Rock. (2) There is a significant lack of buffered phase equilibrium experiments on low-MgO, high-SiO₂ rhyolites, which inhibited our ability to evaluate mafic phenocrysts versus xenocrysts. Moreover, these experiments could be added to the calibration of rhyolite-MELTS, which would expand its range of applicability. (3) Melt inclusions studies to determine volatile contents (H₂O, CO₂, Cl) in Banco Bonito (and other East Fork members) would greatly aid in interpretations of pressure estimates from mineral-barometers.

6 CONCLUSIONS

All post-collapse rhyolites except for Cerro Del Medio and Banco Bonito contain sanidine, anorthoclase/plagioclase, quartz, biotite, hornblende, ±orthopyroxene, ±clinopyroxene, ±zircon, ±apatite, and ±chevkinite. Banco Bonito in this study contains plagioclase, quartz, biotite, hornblende, orthopyroxene, and clinopyroxene, with trace zircon present. We do not find phenocrystic sanidine in our Banco Bonito samples, which contrasts with studies in the literature and suggests the Banco Bonito flow is heterogeneous or that the eruptive temperature of our sample is higher than that of sani-

dine saturation. Further, Banco Bonito is the only rhyolite to contain crystalline inclusions of a biotite-granitoid and spinel-gabbro. For most samples, microprobe analyses show that anorthoclase, plagioclase, sanidine, biotite, hornblende, ilmenite, and magnetite span a relatively narrow range in composition within each rhyolite. A majority of crystals in the HSRs are phenocrystic based on an evaluation of mineral textures, a comparison of mineral compositions with those grown in phase equilibrium experiments from the literature, and general agreement between temperatures from a set of thermometers applied to ilmenite and magnetite, hornblende, and clinopyroxene. We find frequent evidence of inherited crystals in the younger LSRs, which have xenocrystic orthopyroxene and anorthoclase with calcic cores (San Antonio rhyolite) and plagioclase with calcic, sieve textured cores (Banco Bonito rhyolite).

The average pre-eruptive temperatures (based on Fe-Ti oxides, hornblende, and clinopyroxene), oxygen fugacities (based on Fe-Ti oxides), and H₂O contents (derived from plagioclase-hygrometry) of the post-collapse rhyolites range from 742-824 °C, -0.1 to +1.3 Δ NNO, and 4.4-6.0 wt% H_2O , respectively. Average storage pressures based on pure-H₂O solubility and hornblende barometry range from 130–376 MPa or ~5-14 km depth. The intensive variables of the postcollapse rhyolites follow a trend where the HSRs have colder pre-eruptive temperatures than the LSRs, and the youngest LSR records a wide range of storage pressures (82–376 MPa or ~3-14 km when considering an upper crustal density of $2700\,\mathrm{kg}\,\mathrm{m}^{-3}$) overlapping with the HSRS common depths of ~5-7 km (130-194 MPa). The most noticeable change between the eruption of the UBT and the post-collapse rhyolites is the shift to oxidizing conditions, despite the close temporal proximity and common magmatic storage depths. We find the best explanation to account for the change in oxidation state, along with isotopic and geochronologic results reported in the literature, is that the UBT accumulates at the same preeruptive pressure as the post-collapse rhyolites, but is generated from a unique, reduced source.

Finally, we note several areas of future work that would improve interpretation of the post-collapse rhyolites at Valles Caldera: (1) collection of trace element analyses on matrix glasses of rhyolite to assess heterogeneity; (2) addition of buffered phase equilibrium studies on low-MgO, high-SiO $_2$ liquids; and (3) melt inclusion studies of post-collapse rhyolites, especially the East Fork Member, to understand results of mineral-barometry.

AUTHOR CONTRIBUTIONS

This work is a joint effort in data collection and writing between Magdalen A. Grismer and Laura E. Waters.

ACKNOWLEDGEMENTS

This work was supported by NSF-2022465 and startup funds from the New Mexico Institute of Mining and Technology. We thank Matt Zimmerer for providing additional samples from the New Mexico Bureau of Geology and Mineral Resources collection. We thank Robert Palmer for generously providing samples from the Valles Caldera National Preserve

collection during a time when we could not acquire our own. We thank Nels Iverson and Lynn Heizler for their support and expertise on the microprobe. We are also grateful to Phil Kyle and Ben Ellis for their initial feedback and continued enthusiasm for this project. We thank Joe Boro, an anonymous reviewer, and Kayla Iacovino for their reviews and feedback which helped this manuscript immensely. We would also like to acknowledge that this work took place using samples from the ancestral lands of the Rìo Grande Pueblo communities including Jèmez, Zìa, Santa Ana, San Felipe, Cochitì, Santo Domingo, Tesuque, San Ildefonso, Santa Clara, and San Juan; the west-central New Mexico Pueblo of Zuni; the northeastern Arizona Hopi Tribe; the Dinè of the Navajo Nation Four Corners Region; the Jicarilla Apache Tribe of northwestern New Mexico; and the Ute people in Colorado [Merlan and Anschuetz 2007].

DATA AVAILABILITY

Sampling notes are available in Supplementary Material 1. All data personally collected in this work are available in Supplementary Material 2; additional figures and images are available in Supplementary Material 3.

COPYRIGHT NOTICE

© The Author(s) 2024. This article is distributed under the terms of the Creative Commons Attribution 4.0 International License, which permits unrestricted use, distribution, and reproduction in any medium, provided you give appropriate credit to the original author(s) and the source, provide a link to the Creative Commons license, and indicate if changes were made.

REFERENCES

- Acosta-Vigil, A., D. London, and G. B. Morgan (2006). "Experiments on the kinetics of partial melting of a leucogranite at 200 MPa H₂O and 690–800°C: compositional variability of melts during the onset of H₂O-saturated crustal anatexis". *Contributions to Mineralogy and Petrology* 151(5), pages 539–557. DOI: 10.1007/s00410-006-0081-8.
- Almeev, R. R., T. Bolte, B. P. Nash, F. Holtz, M. Erdmann, and H. E. Cathey (2012). "High-temperature, low-H₂O silicic magmas of the Yellowstone hotspot: an experimental study of rhyolite from the Bruneau-Jarbidge Eruptive Center, Central Snake River Plain, USA". *Journal of Petrology* 53(9), pages 1837–1866. DOI: 10.1093/petrology/egs035.
- Almeev, R. R., F. Holtz, A. A. Ariskin, and J.-I. Kimura (2013). "Storage conditions of Bezymianny Volcano parental magmas: results of phase equilibria experiments at 100 and 700 MPa". *Contributions to Mineralogy and Petrology* 166(5), pages 1389–1414. DOI: 10.1007/s00410-013-0934-x.
- Andersen, D. J., D. H. Lindsley, and P. M. Davidson (1993). "QUILF: a pascal program to assess equilibria among Fe-Mg-Mn-Ti oxides, pyroxenes, olivine, and quartz". *Computers & Geosciences* 19(9), pages 1333–1350. DOI: 10.1016/0098-3004(93)90033-2.
- Andújar, J., F. Costa, J. Martí, J. Wolff, and M. Carroll (2008). "Experimental constraints on pre-eruptive conditions of

- phonolitic magma from the caldera-forming El Abrigo eruption, Tenerife (Canary Islands)". Chemical Geology 257(3-4), pages 173–191. Doi: 10.1016/j.chemgeo.2008.08.012. Andújar, J., F. Costa, and B. Scaillet (2013). "Storage conditions and eruptive dynamics of central versus flank eruptions in volcanic islands: the case of Tenerife (Canary Islands, Spain)". Journal of Volcanology and Geothermal Research 260, pages 62–79. Doi: 10.1016/j.jvolgeores. 2013.05.004.
- Bacon, C. R. and M. M. Hirschmann (1988). "Mg/Mn partitioning as a test for equilibrium between coexisting Fe-Ti oxides". *American Mineralogist* 73(1-2), pages 57–61.
- Balsley, S. D. (1988). The petrology and geochemistry of the Tshirege member of the Bandelier Tuff, Jemez mountains Volcanic field, New Mexico, USA. The University of Texas at Arlington.
- Befus, K. S. and J. E. Gardner (2016). "Magma storage and evolution of the most recent effusive and explosive eruptions from Yellowstone Caldera". Contributions to Mineralogy and Petrology 171(4). DOI: 10.1007/s00410-016-1244-x.
- Bell, A. S. and A. Simon (2011). "Experimental evidence for the alteration of the $\mathrm{Fe^{3+}/\Sigma Fe}$ of silicate melt caused by the degassing of chlorine-bearing aqueous volatiles". *Geology* 39(5), pages 499–502. DOI: 10.1130/g31828.1.
- Bindeman, I. N. and J. W. Valley (2000). "Formation of low-δ¹⁸O rhyolites after caldera collapse at Yellowstone, Wyoming, USA". *Geology* 28(8), page 719. DOI: 10.1130/0091-7613(2000)28<719:folrac>2.0.co;2.
- Bindeman, I. N., K. E. Watts, A. K. Schmitt, L. A. Morgan, and P. W. Shanks (2007). "Voluminous low $\delta^{18}O$ magmas in the late Miocene Heise volcanic field, Idaho: implications for the fate of Yellowstone hotspot calderas". *Geology* 35(11), page 1019. DOI: 10.1130/g24141a.1.
- Blatter, D. L. and I. S. Carmichael (2001). "Hydrous phase equilibria of a Mexican high-silica andesite: a candidate for a mantle origin?" *Geochimica et Cosmochimica Acta* 65(21), pages 4043–4065. DOI: 10.1016/s0016-7037(01)00708-6.
- Blatter, D. L., T. W. Sisson, and W. B. Hankins (2013). "Crystallization of oxidized, moderately hydrous arc basalt at midto lower-crustal pressures: implications for andesite genesis". *Contributions to Mineralogy and Petrology* 166(3), pages 861–886. DOI: 10.1007/s00410-013-0920-3.
- Bolte, T., F. Holtz, R. Almeev, and B. Nash (2015). "The Blacktail Creek Tuff: an analytical and experimental study of rhyolites from the Heise volcanic field, Yellowstone hotspot system". *Contributions to Mineralogy and Petrology* 169(2). DOI: 10.1007/s00410-015-1112-0.
- Boro, J. R., J. A. Wolff, and O. K. Neill (2020). "Anatomy of a recharge magma: hornblende dacite pumice from the rhyolitic Tshirege Member of the Bandelier Tuff, Valles Caldera, New Mexico, USA". Contributions to Mineralogy and Petrology 175(10). DOI: 10.1007/s00410-020-01725-W.
- Broxton, D., G. WoldeGabriel, L. Peters, J. Budahn, and G. Luedemann (2007). "Pliocene volcanic rocks of the Tschicoma Formation, eastcentral Jemez volcanic field: Chemistry, petrography, and age constraints". 58th Field Conference, Guidebook, pages 284–295.

- Brugger, C. R., A. D. Johnston, and K. V. Cashman (2003). "Phase relations in silicic systems at one-atmosphere pressure". *Contributions to Mineralogy and Petrology* 146(3), pages 356–369. DOI: 10.1007/s00410-003-0503-9.
- Candela, P. A. (1986). "The evolution of aqueous vapor from silicate melts: effect on oxygen fugacity". *Geochimica et Cosmochimica Acta* 50(6), pages 1205–1211. DOI: 10.1016/0016-7037(86)90403-5.
- Carmichael, I. S. and M. Ghiorso (1990). "The effect of oxygen fugacity on the redox state of natural liquids and their crystallizing phases". *Reviews in Mineralogy and Geochemistry* 24(1), pages 191–212.
- Carmichael, I. S. E., J. Nicholls, F. Spera, B. J. Wood, and S. Nelson (1977). "High-temperature properties of silicate liquids: applications to the equilibration and ascent of basic magma". Philosophical Transactions of the Royal Society of London. Series A, Mathematical and Physical Sciences 286(1336), pages 373–431. DOI: 10.1098/rsta.1977.0124.
- Castro, J. M., C. I. Schipper, S. P. Mueller, A. S. Militzer, A. Amigo, C. S. Parejas, and D. Jacob (2013). "Storage and eruption of near-liquidus rhyolite magma at Cordón Caulle, Chile". *Bulletin of Volcanology* 75(4). DOI: 10.1007/s00445-013-0702-9.
- Cole, J., D. Milner, and K. Spinks (2005). "Calderas and caldera structures: a review". *Earth-Science Reviews* 69(1–2), pages 1–26. DOI: 10.1016/j.earscirev.2004.06.004.
- Cook, G. W., J. A. Wolff, and S. Self (2016). "Estimating the eruptive volume of a large pyroclastic body: the Otowi Member of the Bandelier Tuff, Valles caldera, New Mexico". *Bulletin of Volcanology* 78(2). DOI: 10.1007/s00445-016-1000-0.
- Coombs, M. L. and J. E. Gardner (2001). "Shallow-storage conditions for the rhyolite of the 1912 eruption at Novarupta, Alaska". *Geology* 29(9), page 775. DOI: 10.1130/0091-7613(2001)029<0775:sscftr>2.0.co;2.
- Couch, S., C. Harford, R. Sparks, and M. Carroll (2003). "Experimental constraints on the conditions of formation of highly calcic plagioclase microlites at the Soufrire Hills Volcano, Montserrat". *Journal of Petrology* 44(8), pages 1455–1475. DOI: 10.1093/petrology/44.8.1455.
- De Angelis, S., J. Larsen, M. Coombs, A. Dunn, and L. Hayden (2015). "Amphibole reaction rims as a record of pre-eruptive magmatic heating: an experimental approach". *Earth and Planetary Science Letters* 426, pages 235–245. DOI: 10.1016/j.epsl.2015.06.051.
- Droop, G. (1987). "A general equation for estimating Fe³⁺ concentrations in ferromagnesian silicates and oxides from microprobe analyses, using stoichiometric criteria". *Mineralogical magazine* 51(361), pages 431–435.
- Dunbar, N. W. and R. L. Hervig (1992). "Volatile and trace element composition of melt inclusions from the Lower Bandelier Tuff: implications for magma chamber processes and eruptive style". *Journal of Geophysical Research:* Solid Earth 97(B11), pages 15151–15170. DOI: 10.1029/92jb01340.
- Eichler, C. M. and T. L. Spell (2020). "Petrogenesis of three East Fork Member rhyolites of the Jemez volcanic field, Valles

- caldera, New Mexico, USA". Journal of Volcanology and Geothermal Research 389, page 106706. DOI: 10.1016/j.jvolgeores.2019.106706.
- Fabbrizio, A. and M. R. Carroll (2008). "Experimental constraints on the differentiation process and pre-eruptive conditions in the magmatic system of Phlegraean Fields (Naples, Italy)". Journal of Volcanology and Geothermal Research 171(1-2), pages 88–102. DOI: 10.1016/j.jvolgeores.2007.11.002.
- Gardner, J. E., M. Rutherford, S. Carey, and H. Sigurdsson (1995). "Experimental constraints on pre-eruptive water contents and changing magma storage prior to explosive eruptions of Mount St Helens volcano". *Bulletin of Volcanology* 57(1), pages 1–17. DOI: 10.1007/bf00298703.
- Gardner, J. E., K. S. Befus, G. A. R. Gualda, and M. S. Ghiorso (2014). "Experimental constraints on rhyolite-MELTS and the Late Bishop Tuff magma body". Contributions to Mineralogy and Petrology 168(2). DOI: 10.1007/s00410-014-1051-1.
- Gardner, J. N., F. Goff, S. Garcia, and R. C. Hagan (1986). "Stratigraphic relations and lithologic variations in the Jemez volcanic field, New Mexico". *Journal of Geophysical Research: Solid Earth* 91(B2), pages 1763–1778. DOI: 10.1029/JB091iB02p01763.
- Gardner, J. N., F. Goff, S. Kelley, and E. Jacobs (2010). "Rhyolites and associated deposits of the Valles-Toledo caldera complex". *New Mexico Geology* 32(1), pages 3–18.
- Gerke, T. L., A. I. Kilinc, and R. O. Sack (2005). "Ti-content of high-Ca pyroxenes as a petrogenetic indicator: an experimental study of mafic alkaline rocks from the Mt. Erebus volcanic region, Antarctica". Contributions to Mineralogy and Petrology 148(6), pages 735–745. DOI: 10.1007/s00410-004-0636-5.
- Geshi, N. (2020). "Volcanological challenges to understanding explosive large-scale eruptions". *Earth, Planets and Space* 72(1). DOI: 10.1186/s40623-020-01222-1.
- Ghiorso, M. S. and B. W. Evans (2008). "Thermodynamics of rhombohedral oxide solid solutions and a revision of the Fe-Ti two-oxide geothermometer and oxygen-barometer". *American Journal of Science* 308(9), pages 957–1039. DOI: 10.2475/09.2008.01.
- Ghiorso, M. S. and G. A. Gualda (2015). "An H₂O-CO₂ mixed fluid saturation model compatible with rhyolite-MELTS". Contributions to Mineralogy and Petrology 169, pages 1–30. DOI: 10.1007/s00410-015-1141-8.
- Girard, G. and J. Stix (2009). "Magma recharge and crystal mush rejuvenation associated with early post-collapse Upper Basin Member Rhyolites, Yellowstone Caldera, Wyoming". *Journal of Petrology* 50(11), pages 2095–2125. DOI: 10.1093/petrology/egp070.
- Goff, F. (2010). "The Valles caldera: New Mexico's supervolcano". New Mexico Earth Matters 10(1), pages 1–4.
- Goff, F., J. N. Gardner, S. L. Reneau, S. A. Kelley, K. A. Kempter, and J. R. Lawrence (2011). *Geologic map of the Valles caldera, Jemez Mountains, New Mexico*. Volume 79. scale 1, page 50.

- Goff, F., R. Warren, C. J. Goff, and N. Dunbar (2014). "Eruption of reverse-zoned upper Tshirege Member, Bandelier Tuff from centralized vents within Valles caldera, New Mexico". *Journal of Volcanology and Geothermal Research* 276, pages 82–104. DOI: 10.1016/j.jvolgeores.2014.02.018.
- Grocke, S. B., B. J. Andrews, and S. L. de Silva (2017). "Experimental and petrological constraints on long-term magma dynamics and post-climactic eruptions at the Cerro Galán caldera system, NW Argentina". *Journal of Volcanology and Geothermal Research* 347, pages 296–311. DOI: 10.1016/j.jvolgeores.2017.09.021.
- Grove, T. L., J. M. Donnelly-Nolan, and T. Housh (1997). "Magmatic processes that generated the rhyolite of Glass Mountain, Medicine Lake Volcano, N. California". *Contributions to Mineralogy and Petrology* 127(3), pages 205–223. DOI: 10.1007/s004100050276.
- Grove, T. L., L. T. Elkins-Tanton, S. W. Parman, N. Chatterjee, O. Müntener, and G. A. Gaetani (2003). "Fractional crystallization and mantle-melting controls on calc-alkaline differentiation trends". *Contributions to Mineralogy and Petrology* 145(5), pages 515–533. DOI: 10.1007/s00410-003-0448-z.
- Grove, T. L., D. C. Gerlach, and T. W. Sando (1982). "Origin of calc-alkaline series lavas at Medicine Lake Volcano by fractionation, assimilation and mixing". Contributions to Mineralogy and Petrology 80(2), pages 160–182. DOI: 10.1007/bf00374893.
- Gualda, G. A. R., M. S. Ghiorso, R. V. Lemons, and T. L. Carley (2012). "Rhyolite-MELTS: a modified calibration of MELTS optimized for silica-rich, fluid-bearing magmatic systems". Journal of Petrology 53(5), pages 875–890. DOI: 10.1093/petrology/egr080.
- Hammarstrom, J. M. and E.-a. Zen (1986). "Aluminum in hornblende: an empirical igneous geobarometer". *American mineralogist* 71(11-12), pages 1297–1313.
- Harms, E., J. Gardner, and H.-U. Schmincke (2004). "Phase equilibria of the Lower Laacher See Tephra (East Eifel, Germany): constraints on pre-eruptive storage conditions of a phonolitic magma reservoir". *Journal of Volcanology and Geothermal Research* 134(1–2), pages 125–138. DOI: 10.1016/j.jvolgeores.2004.01.009.
- Heiken, G., F. Goff, J. Stix, S. Tamanyu, M. Shafiqullah, S. Garcia, and R. Hagan (1986). "Intracaldera volcanic activity, Toledo caldera and embayment, Jemez Mountains, New Mexico". *Journal of Geophysical Research: Solid Earth* 91(B2), pages 1799–1815. DOI: 10.1029/JB091iB02p01799.
- Hildreth, W., A. N. Halliday, and R. L. Christiansen (1991). "Isotopic and chemical evidence concerning the genesis and contamination of basaltic and rhyolitic magma beneath the Yellowstone Plateau Volcanic Field". *Journal of Petrology* 32(1), pages 63–138. DOI: 10.1093/petrology/32.1.63.
- Hildreth, W. (2004). "Volcanological perspectives on Long Valley, Mammoth Mountain, and Mono Craters: several contiguous but discrete systems". *Journal of Volcanology and Geothermal Research* 136(3–4), pages 169–198. DOI: 10.1016/j.jvolgeores.2004.05.019.
- Hildreth, W., J. Fierstein, and A. Calvert (2017). "Early post-caldera rhyolite and structural resurgence at Long Val-

- ley Caldera, California". Journal of Volcanology and Geothermal Research 335, pages 1–34. DOI: 10.1016/j.jvolgeores.2017.01.005.
- Hildreth, W. and C. J. N. Wilson (2007). "Compositional zoning of the Bishop Tuff". *Journal of Petrology* 48(5), pages 951–999. DOI: 10.1093/petrology/egm007.
- Hollister, L. S., G. Grissom, E. Peters, H. Stowell, and V. Sisson (1987). "Confirmation of the empirical correlation of Al in hornblende with pressure of solidification of calc-alkaline plutons". American mineralogist 72(3-4), pages 231–239.
- Hou, T., R. Botcharnikov, E. Moulas, T. Just, J. Berndt, J. Koepke, Z. Zhang, M. Wang, Z. Yang, and F. Holtz (2021). "Kinetics of Fe-Ti oxide re-equilibration in magmatic systems: implications for thermo-oxybarometry". *Journal of Petrology* 61(11-12). DOI: 10.1093/petrology/egaa116.
- Iacovino, K., S. Matthews, P. E. Wieser, G. M. Moore, and F. Bégué (2021). "VESIcal Part I: An open-source thermodynamic model engine for mixed volatile (H₂O-CO₂) solubility in silicate melts". Earth and Space Science 8(11). DOI: 10.1029/2020ea001584.
- Icenhower, J. and D. London (1995). "An experimental study of element partitioning among biotite, muscovite, and coexisting peraluminous silicic melt at 200 MPa ($\rm H_2O$)". American Mineralogist 80(11-12), pages 1229–1251. DOI: 10. 2138/am-1995-11-1213.
- Juster, T. C., T. L. Grove, and M. R. Perfit (1989). "Experimental constraints on the generation of FeTi basalts, andesites, and rhyodacites at the Galapagos Spreading Center, 85°W and 95°W". Journal of Geophysical Research: Solid Earth 94(B7), pages 9251–9274. DOI: 10.1029/jb094ib07p09251.
- Kelley, S. A., W. C. McIntosh, F. Goff, K. A. Kempter, J. A. Wolff, R. Esser, S. Braschayko, D. Love, and J. N. Gardner (2013). "Spatial and temporal trends in pre-caldera Jemez Mountains volcanic and fault activity". Geosphere 9(3), pages 614–646. DOI: 10.1130/ges00897.1.
- Kress, V. C. and I. S. E. Carmichael (1991). "The compressibility of silicate liquids containing Fe₂O₃ and the effect of composition, temperature, oxygen fugacity and pressure on their redox states". Contributions to Mineralogy and Petrology 108(1-2), pages 82–92. DOI: 10.1007/bf00307328.
- Kuentz, D. C. (1986). The Otowi member of the Bandelier Tuff: a study of the petrology petrography, and geochemistry of an explosive silicic eruption, Jemez Mountains, New Mexico. The University of Texas at Arlington.
- Landi, P., N. Métrich, A. Bertagnini, and M. Rosi (2004). "Dynamics of magma mixing and degassing recorded in plagioclase at Stromboli (Aeolian Archipelago, Italy)". *Contributions to Mineralogy and Petrology* 147(2), pages 213–227. DOI: 10.1007/s00410-004-0555-5.
- Lange, R. A., H. M. Frey, and J. Hector (2009). "A thermodynamic model for the plagioclase-liquid hygrometer/thermometer". *American Mineralogist* 94(4), pages 494–506. DOI: 10.2138/am.2009.3011.
- Larsen, J. F. (2006). "Rhyodacite magma storage conditions prior to the 3430 yBP caldera-forming eruption of Aniakchak volcano, Alaska". Contributions to Mineralogy and Petrology 152(4), pages 523–540. DOI: 10.1007/s00410-006-0121-4.

- Li, X., C. Zhang, H. Behrens, and F. Holtz (2020). "Calculating biotite formula from electron microprobe analysis data using a machine learning method based on principal components regression". *Lithos* 356–357, page 105371. DOI: 10.1016/j.lithos.2020.105371.
- Lukkari, S. and F. Holtz (2007). "Phase relations of a F-enriched peraluminous granite: an experimental study of the Kymi topaz granite stock, southern Finland". Contributions to Mineralogy and Petrology 153(3), pages 273–288. DOI: 10.1007/s00410-006-0146-8.
- Mackwell, S. (1992). "Oxidation kinetics of fayalite (Fe₂SiO₄)". *Physics and Chemistry of Minerals* 19(4). DOI: 10.1007/bf00202311.
- Magnani, M., K. Miller, A. Levander, and K. Karlstrom (2004). "The Yavapai-Mazatzal boundary: A long-lived tectonic element in the lithosphere of southwestern North America". *Geological Society of America Bulletin* 116(9), page 1137. DOI: 10.1130/b25414.1.
- Martel, C., M. Pichavant, J. Bourdier, H. Traineau, F. Holtz, and B. Scaillet (1998). "Magma storage conditions and control of eruption regime in silicic volcanoes: experimental evidence from Mt. Pelée". *Earth and Planetary Science Letters* 156(1–2), pages 89–99. DOI: 10.1016/s0012-821x(98) 00003-x.
- Martel, C. (2012). "Eruption dynamics inferred from microlite crystallization experiments: application to Plinian and dome-forming eruptions of Mt. Pelee (Martinique, Lesser Antilles)". *Journal of Petrology* 53(4), pages 699–725. DOI: 10.1093/petrology/egr076.
- Martel, C., R. Champallier, G. Prouteau, M. Pichavant, L. Arbaret, H. Balcone-Boissard, G. Boudon, P. Boivin, J.-L. Bourdier, and B. Scaillet (2013). "Trachyte phase relations and implication for magma storage conditions in the Chaine des Puys (French Massif Central)". Journal of Petrology 54(6), pages 1071–1107. DOI: 10.1093/petrology/egt006.
- Martel, C. and B. C. Schmidt (2003). "Decompression experiments as an insight into ascent rates of silicic magmas". Contributions to Mineralogy and Petrology 144(4), pages 397–415. DOI: 10.1007/s00410-002-0404-3.
- Marxer, F. and P. Ulmer (2019). "Crystallisation and zircon saturation of calc-alkaline tonalite from the Adamello Batholith at upper crustal conditions: an experimental study". Contributions to Mineralogy and Petrology 174(10). DOI: 10.1007/s00410-019-1619-x.
- Mason, B. G., D. M. Pyle, and C. Oppenheimer (2004). "The size and frequency of the largest explosive eruptions on Earth". *Bulletin of Volcanology* 66(8), pages 735–748. DOI: 10.1007/s00445-004-0355-9.
- Merlan, T. and K. F. Anschuetz (2007). "More than a scenic mountain landscape: Valles Caldera National Preserve land use history." Fort Collins, CO: U.S. Department of Agriculture, Forest Service, Rocky Mountain Research Station. Chapter History of the Baca Location No. 1, pages 31–48.
- Meszaros, N. F., J. E. Gardner, M. J. Zimmerer, and K. S. Befus (2023). "Ten thousand years of magma storage preceding the last caldera-forming eruption of the Bandelier Magmatic

- System, New Mexico, USA". *Journal of Petrology* 64(10). DOI: 10.1093/petrology/egad067.
- Molina, J., J. Moreno, A. Castro, C. Rodriguez, and G. Fershtater (2015). "Calcic amphibole thermobarometry in metamorphic and igneous rocks: new calibrations based on plagioclase/amphibole Al-Si partitioning and amphibole/liquid Mg partitioning". *Lithos* 232, pages 286–305. DOI: 10.1016/j.lithos.2015.06.027.
- Mutch, E. J. F., J. D. Blundy, B. C. Tattitch, F. J. Cooper, and R. A. Brooker (2016). "An experimental study of amphibole stability in low-pressure granitic magmas and a revised Alin-hornblende geobarometer". *Contributions to Mineralogy and Petrology* 171(10). DOI: 10.1007/s00410-016-1298-9.
- Nasholds, M. W. and M. J. Zimmerer (2022). "High-precision ⁴⁰Ar/³⁹Ar geochronology and volumetric investigation of volcanism and resurgence following eruption of the Tshirege Member, Bandelier Tuff, at the Valles caldera". *Journal of Volcanology and Geothermal Research* 431, page 107624. DOI: 10.1016/j.jvolgeores.2022.107624.
- Phillips, E. H., F. Goff, P. R. Kyle, W. C. McIntosh, N. W. Dunbar, and J. N. Gardner (2007). "The ⁴⁰Ar/³⁹Ar age constraints on the duration of resurgence at the Valles caldera, New Mexico". *Journal of Geophysical Research: Solid Earth* 112(B8). DOI: 10.1029/2006jb004511.
- Pichavant, M., B. Mysen, and R. Macdonald (2002). "Source and H₂O content of high-MgO magmas in island arc settings: an experimental study of a primitive calc-alkaline basalt from St. Vincent, Lesser Antilles arc". Geochimica et Cosmochimica Acta 66(12), pages 2193–2209. DOI: 10.1016/s0016-7037(01)00891-2.
- Pietranik, A., F. Holtz, J. Koepke, and J. Puziewicz (2009). "Crystallization of quartz dioritic magmas at 2 and 1 kbar: experimental results". *Mineralogy and Petrology* 97(1–2), pages 1–21. DOI: 10.1007/s00710-009-0070-5.
- Putirka, K. (2008). "Thermometers and barometers for volcanic systems". Reviews in Mineralogy and Geochemistry 69(1), pages 61–120. DOI: 10.2138/rmg.2008.69.3.
- (2016). "Amphibole thermometers and barometers for igneous systems and some implications for eruption mechanisms of felsic magmas at arc volcanoes". American Mineralogist 101(4), pages 841–858. DOI: 10.2138/am-2016-5506.
- Rader, E. L. and J. F. Larsen (2013). "Experimental phase relations of a low MgO Aleutian basaltic andesite at $\rm XH_2O$ = 0.7–1". Contributions to Mineralogy and Petrology 166, pages 1593–1611. DOI: 10.1007/s00410-013-0944-8.
- Ren, M. and D. Parker (2019). "Composition variation and eruption dynamics of the El Cajete Series, Valles Caldera, New Mexico". International Journal of Earth & Environmental Sciences 4(1). DOI: 10.15344/2456-351x/2019/163.
- Ricketts, J. W., S. A. Kelley, K. E. Karlstrom, B. Schmandt, M. S. Donahue, and J. van Wijk (2016). "Synchronous opening of the Rio Grande rift along its entire length at 25–10 Ma supported by apatite (U-Th)/He and fission-track thermochronology, and evaluation of possible driving mechanisms". Geological Society of America Bulletin 128(3-4), pages 397–424. DOI: 10.1130/b31223.1.

- Righter, K. and I. S. E. Carmichael (1996). "Phase equilibria of phlogopite lamprophyres from western Mexico: biotite-liquid equilibria and P-T estimates for biotite-bearing igneous rocks". Contributions to Mineralogy and Petrology 123(1), pages 1–21. DOI: 10.1007/s004100050140.
- CD-ROM working group (2002). "Structure and evolution of the lithosphere beneath the Rocky Mountains: initial results from the CD-ROM experiment". *GSA today* 12(3), pages 4–10. DOI: 10.1130/1052-5173(2002)012<0004:SAEOTL>2.0.C0;2.
- Romano, P., J. Andújar, B. Scaillet, N. Romengo, I. di Carlo, and S. G. Rotolo (2018). "Phase equilibria of Pantelleria trachytes (Italy): constraints on pre-eruptive conditions and on the metaluminous to peralkaline transition in silicic magmas". Journal of Petrology 59(3), pages 559–588. DOI: 10.1093/petrology/egy037.
- Romano, P., B. Scaillet, J. C. White, J. Andújar, I. Di Carlo, and S. G. Rotolo (2020). "Experimental and thermodynamic constraints on mineral equilibrium in pantelleritic magmas". *Lithos* 376–377, page 105793. DOI: 10.1016/j.lithos. 2020.105793.
- Ryan, W. B. F., S. M. Carbotte, J. O. Coplan, S. O'Hara, A. Melkonian, R. Arko, R. A. Weissel, V. Ferrini, A. Goodwillie, F. Nitsche, J. Bonczkowski, and R. Zemsky (2009). "Global multi-resolution topography synthesis". *Geochemistry, Geophysics, Geosystems* 10(3). DOI: 10.1029 / 2008gc002332.
- Sato, H. (2005). "Experimental petrology of the 1991–1995 Unzen dacite, Japan. Part II: Cl/OH partitioning between hornblende and melt and its implications for the origin of oscillatory zoning of hornblende phenocrysts". *Journal of Petrology* 46(2), pages 339–354. DOI: 10.1093/petrology/egh078.
- Scaillet, B. (2003). "Experimental constraints on the relationships between peralkaline rhyolites of the Kenya Rift Valley". *Journal of Petrology* 44(10), pages 1867–1894. DOI: 10.1093/petrology/egg062.
- Scaillet, B. and B. W. Evans (1999). "The 15 June 1991 eruption of Mount Pinatubo. I. Phase equilibria and pre-eruption *P-T-fO₂-fH₂O* conditions of the dacite magma". *Journal of Petrology* 40(3), pages 381–411. DOI: 10.1093/petroj/40.3.381.
- Self, S., D. Kircher, and J. Wolff (1988). "The El Cajete Series, Valles Caldera, New Mexico". Journal of Geophysical Research: Solid Earth 93(B6), pages 6113–6127. DOI: 10.1029/JB093iB06p06113.
- Shaw, C. A. (1999). "The Yavapai-Mazatzal crustal boundary in the Southern Rocky Mountains". *Rocky Mountain Geology* 34(1), pages 37–52. DOI: 10.2113/34.1.37.
- Skuba, C. E. (1990). Strontium, niobium, lead, and oxygen isotopic constraints on the genesis and evolution of the Bandelier Tuff. The University of Texas at Arlington.
- Smith, R. L. and R. A. Bailey (1968). "Resurgent cauldrons". *Studies in Volcanology*. Geological Society of America, pages 613–662. DOI: 10.1130/mem116-p613.
- Speer, J. A. (1987). "Evolution of magmatic AFM mineral assemblages in granitoid rocks; the hornblende + melt = biotite reaction in the Liberty Hill Pluton, South Carolina". *American Mineralogist* 72(9-10), pages 863–878.

- Spell, T. L., I. McDougall, and A. P. Doulgeris (1996). "Cerro Toledo Rhyolite, Jemez Volcanic Field, New Mexico: ⁴⁰Ar/³⁹Ar geochronology of eruptions between two caldera-forming events". *Geological Society of America Bulletin* 108(12), pages 1549–1566. DOI: 10.1130/0016–7606(1996)108<1549:CTRJVF>2.3.CO;2.
- Spell, T. L. and T. M. Harrison (1993). "⁴⁰Ar/³⁹Ar geochronology of Post-Valles Caldera Rhyolites, Jemez Volcanic Field, New Mexico". *Journal of Geophysical Research: Solid Earth* 98(B5), pages 8031–8051. DOI: 10.1029/92jb01786.
- Spell, T. L. and P. R. Kyle (1989). "Petrogenesis of Valle Grande Member rhyolites, Valles Caldera, New Mexico: implications for evolution of the Jemez Mountains magmatic system". Journal of Geophysical Research: Solid Earth 94(B8), pages 10379–10396. DOI: 10.1029/jb094ib08p10379.
- Spell, T. L., P. R. Kyle, M. F. Thirlwall, and A. R. Campbell (1993). "Isotopic and geochemical constraints on the origin and evolution of postcollapse rhyolites in the Valles Caldera, New Mexico". *Journal of Geophysical Research: Solid Earth* 98(B11), pages 19723–19739. DOI: 10.1029/93jb01569.
- Tomiya, A., E. Takahashi, N. Furukawa, and T. Suzuki (2010). "Depth and evolution of a silicic magma chamber: melting experiments on a low-K rhyolite from Usu Volcano, Japan". *Journal of Petrology* 51(6), pages 1333–1354. DOI: 10.1093/petrology/egq021.
- Troch, J., B. S. Ellis, C. Harris, O. Bachmann, and I. N. Bindeman (2020). "Low-6¹⁸O silicic magmas on Earth: a review". *Earth-Science Reviews* 208, page 103299. DOI: 10.1016/j.earscirev.2020.103299.
- Tsuchiyama, A. and E. Takahashi (1983). "Melting kinetics of a plagioclase feldspar". Contributions to Mineralogy and Petrology 84(4), pages 345–354. DOI: 10.1007/bf01160286.
- Villiger, S., P. Ulmer, and O. Muntener (2006). "Equilibrium and fractional crystallization experiments at 0.7 GPa; the effect of pressure on phase relations and liquid compositions of tholeiltic magmas". *Journal of Petrology* 48(1), pages 159–184. DOI: 10.1093/petrology/egl058.
- Waelkens, C. M., J. Stix, E. Eves, C. Gonzalez, and D. Martineau (2022). "H₂O and CO₂ evolution in the Bandelier Tuff sequence reveals multiple and discrete magma replenishments". *Contributions to Mineralogy and Petrology* 177(1). DOI: 10.1007/s00410-021-01866-6.
- Warshaw, C. M. and R. L. Smith (1988). "Pyroxenes and fayalites in the Bandelier Tuff, New Mexico; temperatures and comparison with other rhyolites". *American Mineralogist* 73(9-10), pages 1025–1037.
- Waters, L. and H. Frey (2018). "Crystal-poor rhyolites and rhyodacites from Volcán Tepetiltic, Mexico: evidence for melt formation, crystallization and eruption over short timescales". *Journal of Volcanology and Geothermal Research* 361, pages 36–50. DOI: 10.1016/j.jvolgeores. 2018.08.003.
- Waters, L. E. and B. J. Andrews (2016). "The role of superheating in the formation of Glass Mountain obsidians (Long Valley, CA) inferred through crystallization of sanidine". Contributions to Mineralogy and Petrology 171(10). DOI: 10.1007/s00410-016-1291-3.

- Waters, L. E., B. J. Andrews, and R. A. Lange (2015). "Rapid crystallization of plagioclase phenocrysts in silicic melts during fluid-saturated ascent: phase equilibrium and decompression experiments". *Journal of Petrology* 56(5), pages 981–1006. DOI: 10.1093/petrology/egv025.
- Waters, L. E. and R. A. Lange (2013). "Crystal-poor, multiply saturated rhyolites (obsidians) from the Cascade and Mexican arcs: evidence of degassing-induced crystallization of phenocrysts". Contributions to Mineralogy and Petrology 166(3), pages 731–754. DOI: 10.1007/s00410-013-0919-9.
- (2015). "An updated calibration of the plagioclase-liquid hygrometer-thermometer applicable to basalts through rhyolites". *American Mineralogist* 100(10), pages 2172–2184. DOI: 10.2138/am-2015-5232.
- (2017). "An experimental study of Fe²⁺-MgK_D between orthopyroxene and rhyolite: a strong dependence on H₂O in the melt". Contributions to Mineralogy and Petrology 172(6). DOI: 10.1007/s00410-017-1358-9.
- Wilcock, J., F. Goff, W. G. Minarik, and J. Stix (2013). "Magmatic recharge during the formation and resurgence of the Valles Caldera, New Mexico, USA: evidence from quartz compositional zoning and geothermometry". *Journal of Petrology* 54(4), pages 635–664. DOI: 10.1093/petrology/egs078.
- Wilson, C., B. Houghton, M. McWilliams, M. Lanphere, S. Weaver, and R. Briggs (1995). "Volcanic and structural evolution of Taupo Volcanic Zone, New Zealand: a review". *Journal of Volcanology and Geothermal Research* 68(1–3), pages 1–28. DOI: 10.1016/0377-0273(95)00006-g.
- Wolff, J. A. and J. N. Gardner (1995). "Is the Valles Caldera entering a new cycle of activity?" *Geology* 23(5), page 411. DOI: 10.1130/0091-7613(1995)023<0411:itvcea>2.3. co;2.
- Wolff, J. A. and F. C. Ramos (2014). "Processes in calderaforming high-silica rhyolite magma: Rb-Sr and Pb isotope systematics of the Otowi Member of the Bandelier Tuff,

- Valles Caldera, New Mexico, USA". *Journal of Petrology* 55(2), pages 345–375. DOI: 10.1093/petrology/egt070.
- Wolff, J. A., M. C. Rowe, R. Teasdale, J. N. Gardner, F. C. Ramos, and C. E. Heikoop (2005). "Petrogenesis of precaldera mafic lavas, Jemez Mountains Volcanic Field (New Mexico, USA)". Journal of Petrology 46(2), pages 407—439. DOI: 10.1093/petrology/egh082.
- Wolff, J., B. Ellis, F. Ramos, W. Starkel, S. Boroughs, P. Olin, and O. Bachmann (2015). "Remelting of cumulates as a process for producing chemical zoning in silicic tuffs: a comparison of cool, wet and hot, dry rhyolitic magma systems". *Lithos* 236–237, pages 275–286. DOI: 10.1016/j.lithos. 2015.09.002.
- Wolff, J. and F. Ramos (2003). "Pb isotope variations among Bandelier Tuff feldspars: no evidence for a long-lived silicic magma chamber". *Geology* 31(6), page 533. DOI: 10.1130/0091-7613(2003)031<0533:pivabt>2.0.co;2.
- Wolff, J. A., B. S. Ellis, and F. C. Ramos (2011). "Strontium isotopes and magma dynamics: insights from high-temperature rhyolites". *Geology* 39(10), pages 931–934. DOI: 10.1130/g32062.1.
- Wolff, J. A. and J. Neukampf (2022). "Biotite as an indicator of post-eruptive cryptic alteration in the Battleship Rock Ign-imbrite, Valles Caldera, NM, USA". *Bulletin of Volcanology* 84(11). DOI: 10.1007/s00445-022-01609-w.
- Wu, J., S. J. Cronin, M. C. Rowe, J. A. Wolff, S. J. Barker, B. Fu, and S. Boroughs (2021). "Crustal evolution leading to successive rhyolitic supereruptions in the Jemez Mountains volcanic field, New Mexico, USA". *Lithos* 396–397, page 106201. DOI: 10.1016/j.lithos.2021.106201.
- Zimmerer, M. J., J. Lafferty, and M. A. Coble (2016). "The eruptive and magmatic history of the youngest pulse of volcanism at the Valles caldera: implications for successfully dating late Quaternary eruptions". *Journal of Volcanology and Geothermal Research* 310, pages 50–57. DOI: 10.1016/j.jvolgeores.2015.11.021.